Turbulent Dynamics of Buoyant Melt Plumes Adjacent Near-Vertical Glacier Ice

Jonathan D Nash[1], Kaelan Weiss[1], Meagan Elizabeth Wengrove[1], Noah Osman[1], Erin Christine Pettit[1], Ken Zhao[1], Rebecca H. Jackson[2], Jasmine Nahorniak[1], Kyle Jensen[1], Erica Tindal[1], Eric Skyllingstad[3], Nadia Cohen[1], and David A Sutherland[4]

[1]Oregon State University
[2]Rutgers University
[3]Oregon State University, Oregon
[4]University of Oregon

February 23, 2024

Abstract

At marine-terminating glaciers, the interplay between meltwater buoyancy and local currents control turbulent exchanges. Because of challenges in making centimeter-scale measurements at glaciers, turbulent dynamics at near-vertical ice-ocean boundaries are poorly constrained. Here we present the first observations from instruments robotically-bolted to an underwater ice face, and use these to elucidate the tug-of-war between meltwater-derived buoyancy and externally-forced currents in controlling boundary-layer dynamics. Our observations captured two limiting cases of the flow. When external currents are weak, meltwater buoyancy energizes the turbulence and dominates the near-boundary stress. When external currents strengthened, the plume diffused far from the boundary and the associated turbulence decreases. As a result, even relatively weak buoyant melt plumes are as effective as moderate shear flows in delivering heat to the ice. These are the first in-situ observations to demonstrate how buoyant melt plumes energize near-boundary turbulence, and why their dynamics are critical in predicting ice melt.

Turbulent Dynamics of Buoyant Melt Plumes Adjacent Near-Vertical Glacier Ice

Jonathan D Nash[1], Kaelan Weiss[1], Meagan E Wengrove[1], Noah Osman[1], Erin C Pettit[1], Ken Zhao[1,2], Rebecca H Jackson[3], Jasmine Nahorniak[1], Kyle Jensen[1], Erica Tindal[1], Eric D Skyllingstad[1], Nadia Cohen[1] and David Sutherland[4]

[1]Oregon State University
[2]University of Southern California, San Diego
[3]Rutgers University
[4]University of Oregon

Key Points:

- Robotic observations at a submerged near-vertical iceberg face capture turbulent dynamics of buoyant melt plumes and background currents
- Buoyant plumes extend 20-50 cm from the boundary, undulate on 100-s periods, and drive horizontal turbulent transports.
- Buoyant plumes can be more effective than horizontal flows in energizing boundary layer turbulence and heat flux.

Corresponding author: Jonathan D. Nash, `Jonathan.Nash+GRL@oregonstate.edu`

Abstract

At marine-terminating glaciers, the interplay between meltwater buoyancy and local currents control turbulent exchanges. Because of challenges in making centimeter-scale measurements at glaciers, turbulent dynamics at near-vertical ice-ocean boundaries are poorly constrained. Here we present the first observations from instruments robotically-bolted to an underwater ice face, and use these to elucidate the tug-of-war between meltwater-derived buoyancy and externally-forced currents in controlling boundary-layer dynamics. Our observations captured two limiting cases of the flow. When external currents are weak, meltwater buoyancy energizes the turbulence and dominates the near-boundary stress. When external currents strengthened, the plume diffused far from the boundary and the associated turbulence decreases. As a result, even relatively weak buoyant melt plumes are as effective as moderate shear flows in delivering heat to the ice. These are the first *in-situ* observations to demonstrate how buoyant melt plumes energize near-boundary turbulence, and why their dynamics are critical in predicting ice melt.

Plain Language Summary

Melting glaciers are projected to produce several inches of sea level rise over the next few decades. Despite this threat, the fundamental fluid dynamics which drive melt at tidewater glaciers remain poorly characterized. This is primarily attributed to challenges associated with measuring the temperature and velocity of ocean water at the submerged cliffs of actively calving glaciers. To this end, we have developed a robotically-deployed instrument that can be bolted to a glacier's face. This instrument is capable of measuring temperature and kinetic energy of ocean waters within a few inches of the ice, representing the first measurements of their kind. Our observations demonstrate the ways in which meltwater at ice boundaries can accelerate melt. In particular, the meltwater tends to be less salty (and hence lighter) than the nearby ocean waters (which are salty, warm and heavy), so the meltwater rises along the ice face, creating an energetic, near boundary flow. With our new measurements, we show that these flows are as important as large-scale currents in providing energy to the ice to fuel melt. We anticipate these data will help our community create more accurate models of ice melt needed to predict the advance or retreat of marine ice cliffs of Greenland, Alaska and Antarctica.

1 Introduction

Directly quantifying the rate of ice-melt at the near-vertical cliffs of marine-terminating glaciers is a challenge due to the boundary's inaccessibility to traditional forms of sampling. The ice melt-process is also complicated because the thermodynamics depend on how local buoyancy production (from melt) combines with the external forcing (temperature T, salinity s, velocity $\vec{u}$) to control energy flow across the ice boundary. The heat flux j_q, for example, is ultimately set by strong thermal gradients near the diffusive scales, which provides buoyant energy that fuels the turbulent energy cascade. In turn this cascade also intensifies the near-boundary thermal gradients that drive melt and supply buoyant energy (Fig. 1A). This feedback loop is at odds with traditional turbulence theory that often assumes isotropy, homogeneity and the ability to separate the spatial scales of energy sources (large) and sinks (small).

At an ice face, we hypothesize that meltwater detaches from the boundary in fine-scale turbulent sweeps, similar to those observed under sea ice (Fer et al., 2004) and in atmospheric boundary layers (Kline et al., 1967), but here producing buoyant energy at the same small scales that dominate viscous dissipation. Meltwater buoyancy thus injects additional momentum at very small scales – near the viscous tail of a downscale turbulent energy cascade likely fueled both by the large-scale buoyant forcing (Xu et al., 2013) alongside a zoo of classic ocean- (Gargett, 1989) and fjord-specific (Bendtsen et al., 2021) turbulence sources. Further complicating the dynamics are the energy exchanges as parcels entrain buoyancy from the background stratification as they move vertically against gravity, which can represent either a source or sink of energy (Magorrian & Wells, 2016; Kimura et al., 2014).

Beneath gently-sloping, near-horizontal ice-ocean interfaces, meltwater buoyancy drives along-ice flow. However, this buoyancy also provides static stability, so turbulent exchanges primarily occur through hydrodynamic instability such as Kelvin-Helmholz billows (Smyth, 1999). In 1984, a comprehensive set of observations of turbulent melt dynamics in the Marginal Ice Zone of the Greenland Sea were acquired (McPhee et al., 1987). McPhee et al. (1987) used these data to create an empirical model to predict melt from T, s, and the turbulent stress τ, which formed the basis for the canonical three-equation melt parameterization (Holland & Jenkins, 1999). Because the stability of the ice permitted detailed, high-accuracy measurements to be obtained, this parameterization (based on ice-melt thermodynamics and three empirical coefficients derived from those experiments), remains the community's primary and only way to predict melt beneath ice shelves (Jenkins et al., 2010) if the relevant flow ($\vec{u}$, T and s) can be prescribed.

As the ice interface approaches vertical, meltwater can generate sufficient buoyancy to become convectively unstable and directly energize turbulence, as demonstrated in the laboratory by Josberger and Martin (1981). Because the entrainment of warm ocean water increases with plume strength, the melt process creates a positive feedback (Fig. 1A) that further energizes the plume to enhance melt. Eckert and Jackson (1950) created a framework for characterizing turbulent free-convection boundary layers adjacent to a heated plate (for air at $Pr = 1$), and their study remains highly relevant today (Parker et al., 2021). However, the ice-melt problem is more complex because: (1) turbulence is generated by both buoyant convection and shear production (Josberger & Martin, 1981; Zhao et al., 2024); (2) melt can be driven by both salinity or thermal gradients, each which diffuse and influence density in different ways (Gade, 1979; Kerr & McConnochie, 2015); (3) vertical gradients of ocean properties (such as density) affect buoyancy production of turbulent energy and the growth of turbulent plumes (i.e., Magorrian and Wells (2016)); and (4) in addition to buoyancy, other sources of velocity like internal waves (Cusack et al., 2023) or mean currents (Jackson et al., 2020; Zhao et al., 2023) affect shear production of turbulent energy.

Theoretical models (i.e. Wells and Worster (2008)) provide a framework to describe plume evolution, but still require turbulence closure derived from laboratory experiments (McConnochie & Kerr, 2017), numerical experiments (Gayen et al., 2016), or observational analogies (McPhee et al., 1987). At the geophysical scale, empirical models have been developed that assume simplified geometries and turbulence closure. For example, Jenkins (2011) used the framework of MacAyeal (1985) to couple buoyant plume theory with the 3-equation melt model (McPhee et al., 1987) to predict the downstream flow evolution. By prescribing an idealized plume geometry, this framework has been used to predict the freshwater distribution from a localized subglacial discharge (Cowton et al., 2015; Carroll et al., 2016) and also for distributed melt (Magorrian & Wells, 2016; Jackson et al., 2020).

To date, there are no experiments analogous to the 1984 sea-ice observations (McPhee et al., 1987) that could be used to constrain the flow and meltrate parameterization for a vertical ice face. In addition to uncertainty in values of drag and transfer coefficients, there is also debate about how to formulate the coupled models themselves. Part of this debate stems from observations of glacier face ablation (Sutherland et al., 2019) and the existence of large-scale meltwater intrusions (Jackson et al., 2020) that imply significantly higher meltrates than predicted with the above theories as applied in their commonly-used forms. It has been suggested that the boundary layers are energized by external currents which increases the turbulent transfer coefficients;

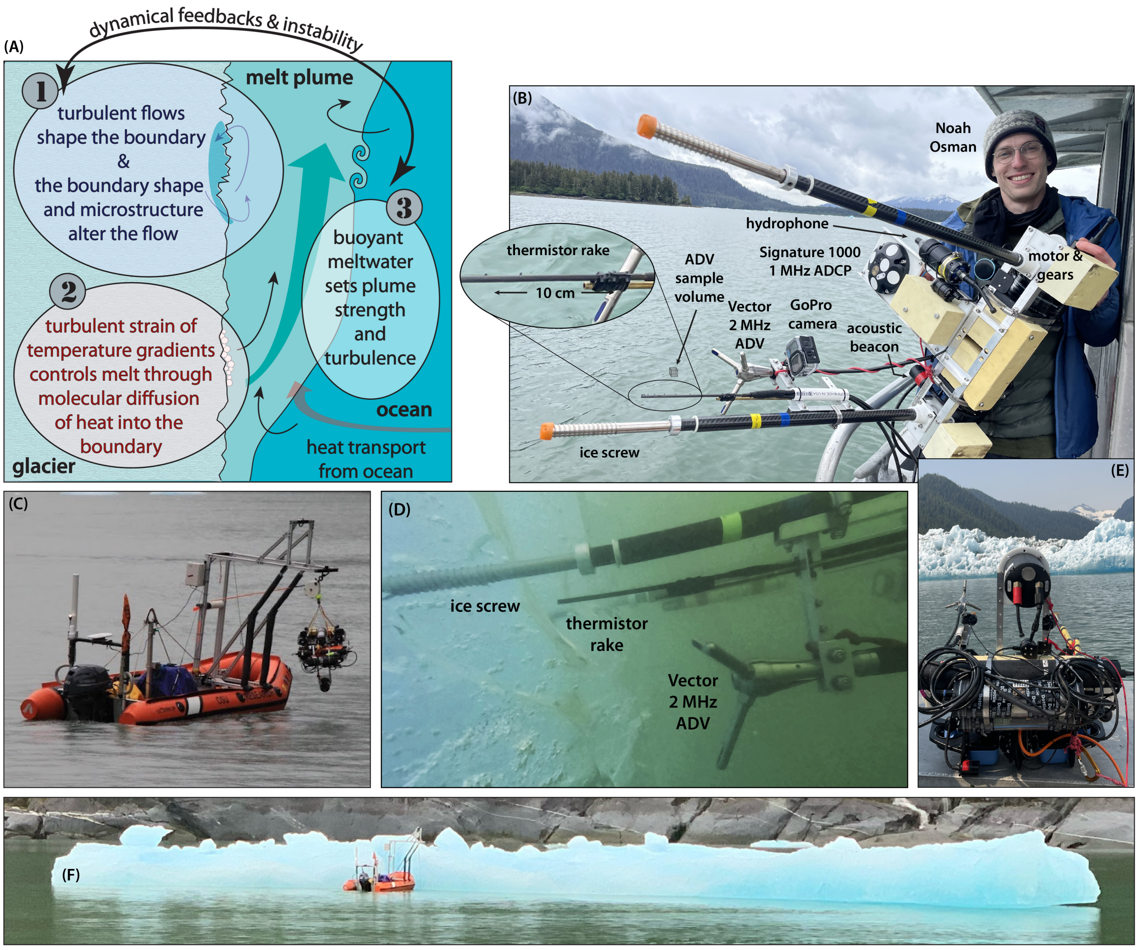

Figure 1. (A) Cartoon illustrates the interplay between (1) ice morphology (2) turbulent and molecular transports across the ocean-ice interface, and (3) melt-driven buoyant plumes that energize the boundary layer. (B) Meltstake sensors are configured to measure these dynamics with minimal disturbance to the flow. (C) Remotely-operated vessel and winched ROV. (D) Meltstake as deployed 12:40 29 May showing ice structure and the sensors' proximity to the interface; the ADCP is outside the frame of view. (E) A Meltstake riding atop the delivery ROV on deck; iceberg from Xeitl Sít' in background. (F) Remote deployment in progress.

anecdotal evidence suggests this is not unreasonable, i.e., Cusack et al. (2023); Slater et al. (2016); Jackson et al. (2020). Other factors – like energy from exploding air bubbles observed in the lab (Wengrove et al., 2023), or ice roughness and channelization observed beneath ice shelves (Stanton et al., 2013; Watkins et al., 2021) – may also be at play here. It is the purpose of this note to describe the first detailed observations of the turbulent flow at a near-vertical glacier-ice face, and to demonstrate how plume buoyancy and external velocities contribute to melt-dynamics. A concurrent paper (Weiss et al, in prep) will extend the analysis of these data to quantify melt rates and assess bias and uncertainty in current melt parameterizations.

2 Methods

2.1 The Glacier Meltstake

The Meltstake is a submarine device (Fig. 1B-F) that is remotely bolted to a near-vertical glacier-ice face to directly measure melt and the spatial structure of near-boundary velocity, temperature and turbulence. It is called a "Meltstake" in analogy to the subaerial ablation stakes used by glaciologists to measure ice accumulation and ablation in the field. It is designed to be a stable platform to observe the flow in a reference frame fixed to the ice and in ways that minimize the system's thermal and hydrodynamic impact on melt dynamics.

The body of the Meltstake is suspended outward from the ice on two, 61-cm long carbon fiber tubes, chosen for their mechanical stiffness and low thermal conductivity $5 \times 10^{-6} \mathrm{m}^2/\mathrm{s}$ (Macias et al., 2019). Ice screws mounted on the ends of these 16-mm diameter tubes turn using Blue Robotics T200 motors at 23:1 reduction. Each screw-assembly rotates within a 25-mm carbon sheath to allow instruments to be rigidly attached at various distances from the ice. A Raspberry Pi "brain" controls drilling power, schedule and underwater communications with a remotely-operated vehicle (ROV) through a long-range 28 kHz Delphis Subsea modem.

The Meltstake is transported to the ice face using a BlueRobotics ROV, equipped with a Ping360 imaging sonar and video camera for underwater navigation. The Meltstake is pinned to the ROV and held in place with a Newton linear actuator. The ROV can be deployed from either a robotic vessel equipped with a remotely-operated winch or a traditional vessel. High-power Ubiquiti Rocket WiFi allows remote operation of the ROV/Meltstake from several kms away using the standard QGroundControl software. Acoustic messages sent from the ROV trigger drill operations. Once the the Meltstake "bites" into the ice, the ROV releases from it. The freed ROV can then monitor the meltstake, request further manual drilling, update the Meltstake's autonomous schedule, or request its release to return to the surface. The unit is rated to 100-m depths, ballasted 10 N buoyant, and has a flasher and GPS/satellite beacon for recovery.

2.2 Experimental setting and measurements

Boundary-layer measurements were made at a freely-floating iceberg with 10-m draft, $\sim$20 km down-fjord from Xeitl Sít'(also called LeConte Glacier) in Southeast Alaska. We deployed the Meltstake on a vertical face of the ice at 6.5-m depth starting at 20:40 UTC, May 29, 2023. As the iceberg melted, we sent acoustic "drill" commands (at 21:39 and 23:05) to advance the Meltstake and move sensors closer to the ice interface. At 23:48 it was released and recovered.

At 00:46, May 30 it was again delivered to the same iceberg at 8.5-m depth, drilled further at 01:46, and released at 02:20.

Velocity was imaged with a 5-beam Nortek 1000 kHz Acoustic Doppler Current Profiler (ADCP) in pulse-coherent mode (4 Hz sampling with 3-4 cm bins). Because of high acoustic backscatter from ice, ADCP data are contaminated by spurious reflections from sidelobes at ranges that exceed the distance of the closest transducer-to-ice distance. We thus attempted to orient the ADCP so that the 4 slant beams encounter the ice at approximately the same range. We use a right-hand coordinate system in which x is along-ice, y is horizontal and positive away from the ice, and z is up. ADCP data were recorded in along-beam coordinates and used for two purposes: (1) opposing beams were combined to determine the bulk vertical (w) and along-ice (u) velocity over the 10-70 cm footprint of the spreading beams; (2) along-beam velocities were used to compute (i) the velocity v from the central beam and (ii) turbulent statistics of the flow using the structure function method of Wiles et al. (2006) as implemented by Thomson et al. (2016). Echo backscatter from a Nortek Vector Acoustic Doppler Velocimeter was used to determine meltrate.

Near-boundary temperature was measured using a thermistor "T-rake," a horizontal array of eight, fast-response thermistors, each exposed downward into the expected flow at distances of 2, 4, 7, 12, 23, 39, 58 and 84 mm from the tip of a carbon tube (Fig. 1B, S1 and supplement). Three fast-response RBR Solos provided additional temperature measurements at 10, 35 and 60 cm from the ice. Salinity was obtained from nearby vertical profiles using a RBR Concerto CTD and ranged from 27.4-28.4 within the $\pm$1-m depth range around each deploment.

3 Observations of buoyancy- and externally-forced boundary layers

Here we examine three time periods that illustrate the range of flow patterns observed (Fig. 2). The first two cases represent a boundary layer energized by the vertical rise of buoyant meltwater, which we term "buoyancy-forced." The third is an example we term "externally-forced," because horizontal velocities were significantly stronger than those of the vertically-rising flows.

Case 1A: Quasi-steady buoyant plume. Shortly after the Meltstake was deployed (at 6.5 m depth, and under weak, $u \sim 1$ cm/s, crossflow conditions), a quasi-steady plume was observed to flow vertically up the ice at 2-4 cm/s within ~ 20 cm of the ice (Fig. 2a-c). During this time, the strongest temperature anomalies (indicative of melt waters) were only observed by sensors within a few millimeters of the T-rake tip, and $\sim$5 cm from the ice.

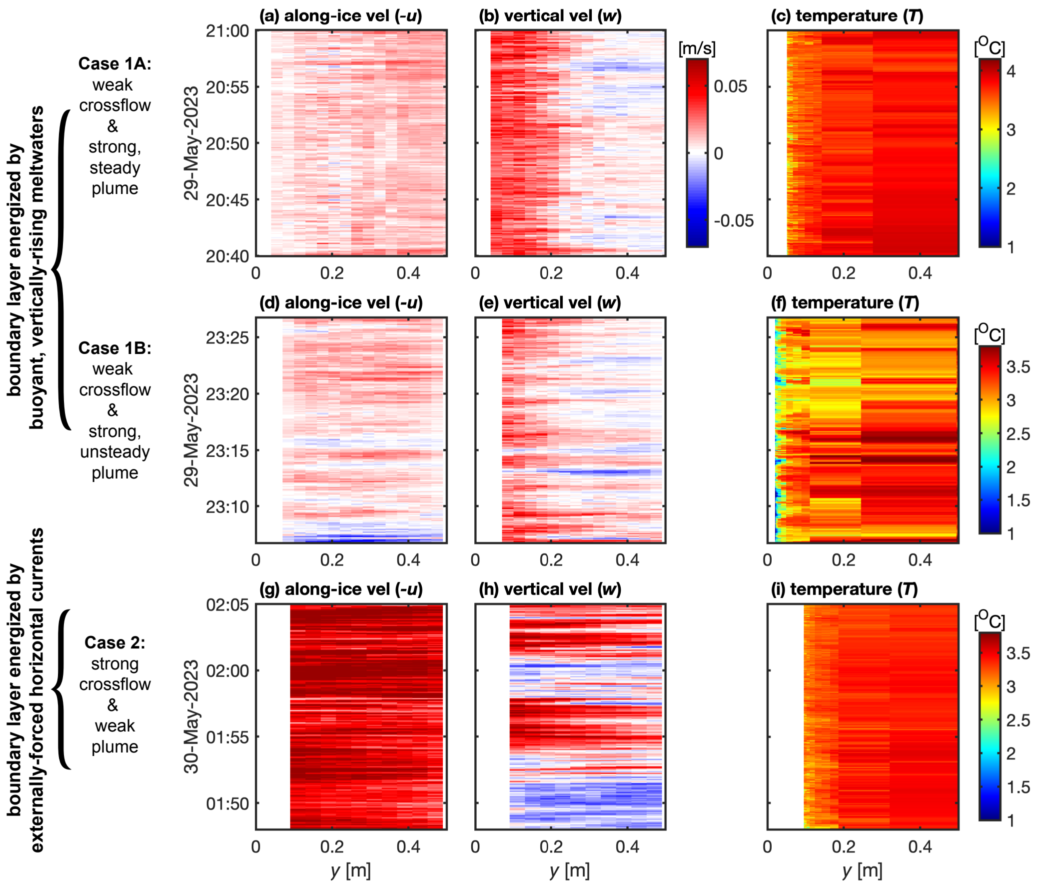

Figure 2. Horizontal, along-ice velocity (a,d,g), vertical velocity (b,e,h), and temperature (c,f,i) within 0.5 m of the ice interface for three twenty-minute periods. Between Case 1A and 1B (at 6.5 m depth), the Meltstake was advanced 6 cm further into the ice, placing the thermistor rake within 2 cm of the ice, but also increasing ADCP sidelobe contamination; Case 2 was a separate deployment at 8.5 m depth. Distance from ice (y) was computed acoustically for $-u$ and w (Weiss et al., 2024) and using equation 3 to determine y_o for $\widehat{T}$; note that the ice melted 3-5 mm during each 20-min period (Weiss et al., 2024), so we treat y independent of time for these plots.

Case 1B: Strongly-undulating buoyant plume. As time evolved the buoyant plume became more variable in time, weakened in magnitude, and decreased in thickness (Fig. 2d-f). The cross-flow also became slightly unsteady (but still weak), undulating with similar timescales as the vertical plume. The Meltstake was also advanced towards the ice between 1A and 1B, yielding T observations within 2 cm from the ice. Temperatures most distant from the ice were observed to increase slightly, and pulses of low-temperature waters were swept 2-10 centimeters from the ice, contrasting the weaker thermal anomalies in case 1A. Far from the boundary ($y > 10$ cm), w alternates sign on ~ 100 second intervals; these pulses appear correlated with temperature. For example, between 23:14 and 23:18 there are several strong vertical velocity reversals that coincide with warm pulses, which could be interpreted as turbulent eddies drawing warm ambient fluid towards the boundary.

Case 2: Strong crossflow. After the Meltstake was released and re-drilled into the ice at 8.5-m depth, the iceberg had moved and tidal flows strengthened, exposing the ice to stronger currents (Fig. 2g-i). At this time, $-u$ averaged 6 cm/s, w was highly variable but upward ($\sim 1-1.5$ cm/s) on average, and both undulated with O(5 min) period; $-u$ and w are correlated and somewhat out-of-phase (the weakest w generally correspond to the largest $-u$). Temperature anomalies (indicating the presence of meltwater) were observed close to the boundary.

4 Character of turbulence in the buoyant plume

To glean insight into turbulent dynamics energized by meltwater buoyancy, we examine the undulating plume case (Case 1B) in more detail. We focus on the 5-10 minutes following drilling (at 23:05) and we look in detail at the 11 individual thermistors in the context of the near-boundary velocities (Fig. 3). During the first 5 minutes, the T-rake was in closest proximity to the ice (see supplement), such that the innermost thermistor (2 mm from the T-rake tip; midnight blue in Fig. 3a) was on average 4 mm from the ice.

These temperature data demonstrate a turbulent melt-and-extrude cycle, whereby the first phase of the eddy draws warm water toward the boundary to initiate melt, and the second phase sweeps the cold meltwaters away from the ice. This pattern can be seen in the traces in Fig. 3a: at times when T rises at the outer sensors, temperatures at the inner sensors cool. For example, at 23:11, 23:14 and 23:16, the 3 outer sensors (red traces in Fig. 3a) warm together, while the inner five sensors (blue-green traces) cool in unison. These cold pulses – which reached as low as 0° C at times – are the signatures of melt emerging from the boundary. Following these (i.e., at

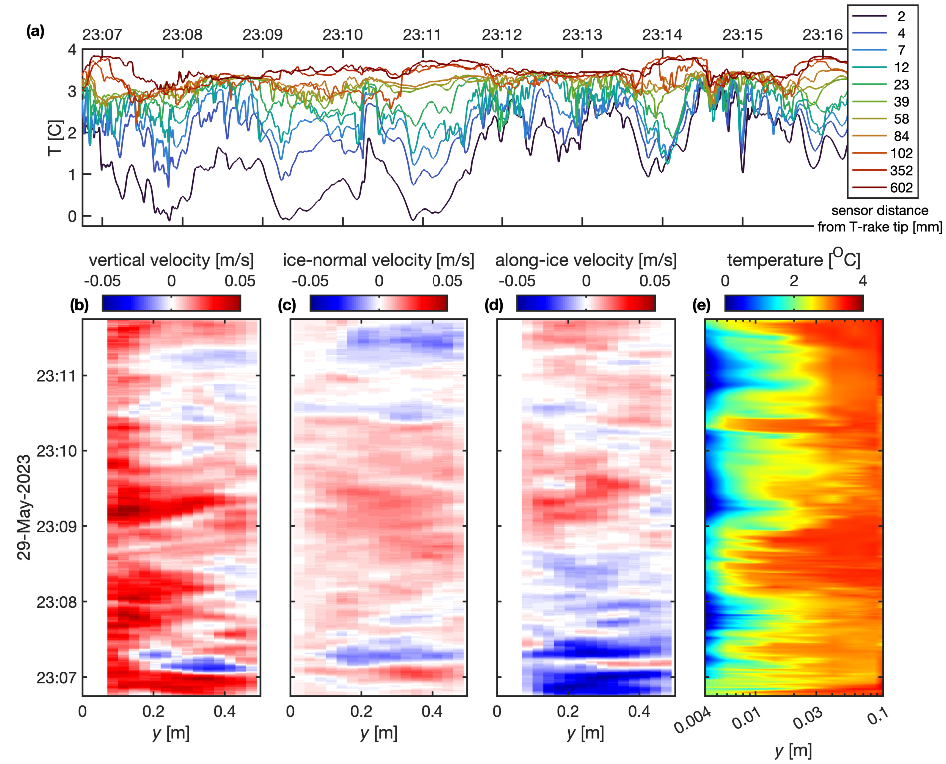

Figure 3. Details of the boundary-layer layer illustrate the dynamics of the unsteady plume: (a) Ten-minute segment of temperature data from the 11 sensors used in Fig. 2f. Lower panels show a zoom-in on the first five minutes of that record on May 29, 2023: (b) vertical velocity, (c) ice-normal velocity (positive/red is away from the ice), (c) along-ice velocity, and (d) temperature, plotted against logarithmic distance coordinates to highlight the smallest scales near the ice boundary. In (c), v is from the ADCP center beam so is least-contaminated by acoustic sidelobes and provides unbiased data almost to the ice surface.

23:12) are periods in which the temperature of all sensors coalesce together, and are the times when warm waters make their closest contact to the ice, presumably temporarily enhance melt.

Anomalies exceeding ~ 1.5 °C (below ambient T_a) were detected 25 mm from the boundary, and coherent across all sensors, indicating a pathway for meltwater to be swept out from the laminar sublayer into the outer layer by turbulence. During these events, the ice-perpendicular velocity (Fig. 3c) was directed away from the face at approximately 1 cm/s, extended 10s of cm from boundary, and varied coherently in all three velocity components. This cycle of perturbations – that brings warm water towards the ice and extrudes cold meltwaters away from the boundary – undulates on 100-s periods, and is the signature of a horizontal eddy-transport of heat that fuels melt.

5 Quantitative differences in flow patterns

To compare the flow characteristics during each of the example time periods, we compute mean profiles of the near-boundary velocity, temperature, turbulent energy and heat transport (Fig. 4). Fits of w and T to empirical functions are used to determine spatial scales, magnitudes and gradients, which we use to determine τ and j_q, both of which are important parameters to predict melt. Consistency between direct turbulence observations and τ derived from Eckert and Jackson (1950)'s self-similar profiles provides confidence in our interpretations.

Velocity: For a convection flow driven by buoyancy from a heated vertical plate, Eckert and Jackson (1950) derived similarity solutions for a Prandtl number ($Pr = 1$) flow. They find the vertical velocity $\widehat{w}$

$$\widehat{w}(\hat{y}) = w_1 \hat{y}^{1/7}(1 - \hat{y})^4. \tag{1}$$

is a function of the nondimensional distance from the wall $\hat{y} = y/\delta$, where δ is assumed to vary slowly in z and represents the distance over which the solution is valid ($\widehat{w} \geq 0$); w_1 is a constant. We use this form to characterize the observed plumes' vertical velocity $w(y)$ by minimizing $\sum (w(y) - \widehat{w}(y))^2$ to determine w_1 and δ over 20-minute durations. For this solution, the peak velocity is $w_{max} = 0.5372 w_1$ and the plume width, defined by $\widehat{w}(L_w)/w_{max} = 1/e$ is $L_w = 0.304\delta$. As shown in Fig. 4(b), these fits represent the data well in the region we have observations, and indicate a factor-of-two increase in plume width ($L_w = 44$ cm) during periods of strong crossflow compared to that during weak ($L_w = 21 - 22$ cm). Because w_{max} decreased for large L_w, the total vertical transport, $Q_{plume} = \int_0^\delta \widehat{w} dy = 0.146 w_1 \delta$ was observed to be similar for each of the three cases: 76, 56 and 78 cm^2/s.

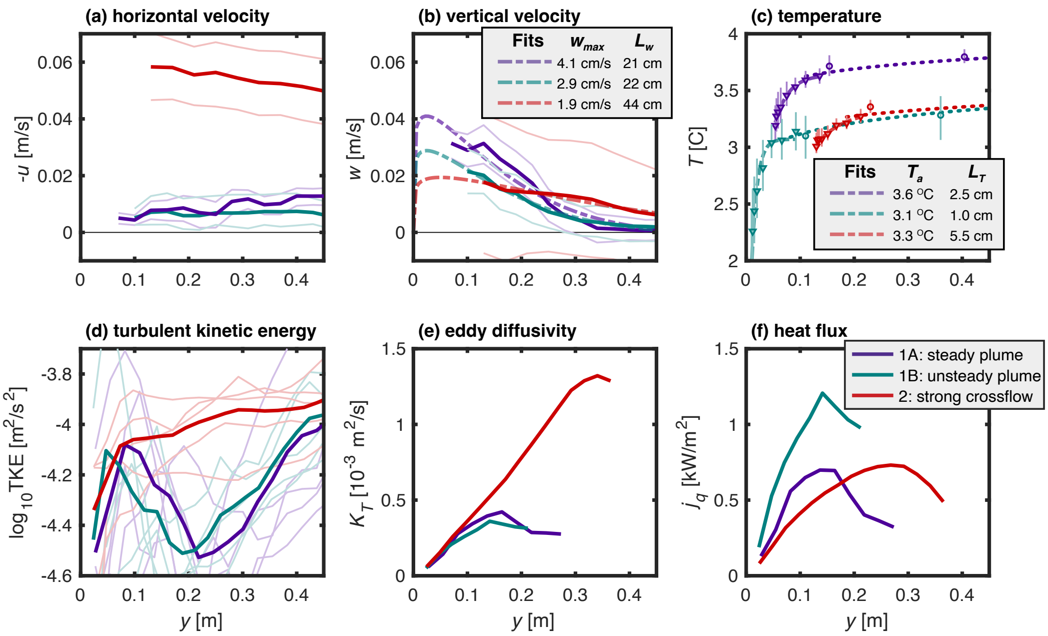

Figure 4. Mean and turbulent characteristics of the observed boundary layers: (a) along-ice velocity $-u$, (b) vertical velocity w, (c) temperature T, (d) turbulent kinetic energy TKE, (e) turbulent diffusivity K_T, and (f) heat flux J_q. Each colored line represents a 20-minute average over the time periods shown in Fig. 2: steady plume (1A, purple), undulating plume (1B, turquoise), strong crossflow (2, red). Thin/light lines in (a-c) define the central 50% of the data. Gaps in (c) separate data from the temperature rake and RBR Solos (separated horizontally by 60 cm and hence responsible for offsets in T). Light dashed lines in (b) and (c) represent eqns. 1, 3 with least-square-fit coefficients as indicated; in (c) fits to eq. 3 use the T-rake data (shown in thick dashed lines) and fits to eq. 2 use the outer 5 T sensors (thin dashed lines). In (d), semi-transparent lines represent estimates of TKE from each of the 5 individual ADCP beams (heavy lines are the means).

Temperature: T-rake timeseries provide temperature and its gradient with sub-centimeter resolution and at close proximity to the ice boundary. Here we use these and Solo data to characterize the thermal boundary layer (see Supplement for details), which we separate into an outer and inner layer.

We begin by considering Eckert and Jackson (1950)'s similarity solution, for which the characteristic lengthscale for $T(y)$ and $w(y)$ assumed the same (δ). In their form (applicable to air ($Pr = 0.7$) and requiring $T = 0$ at the boundary), a substantial temperature gradient (O$\sim$1C/m) is predicted far from the boundary, which is not observed here (Fig. S2). Here we modify their form by introducing ΔT to allow for a lesser temperature drop (relative to ambient T_a) in the outer layer:

$$T = T_a - \Delta T(1 - (y/\delta)^{1/7}). \tag{2}$$

Fits to the outer 5 temperature measurements are roughly consistent with both this form and the logarithmic scaling presented by Tsuji and Nagano (1988) (see Supplement), yeilding a 0.2-0.3 $^\circ$C drop in the outer boundary layer.

Close to the ice, the observed $T(y)$ is inconsistent with (Eckert & Jackson, 1950) eq. (2). Motivated by the early work of Smith (1972) and Tsuji and Nagano (1988), we consider an inner layer shaped by molecular transports and having a different characteristic lengthscale L_T, and arbitrarily assume the following exponential form:

$$\widehat{T}(y) = T_a - (T_a - T_i)e^{-y/L_T}. \tag{3}$$

Here we assume the ice temperature $T_i = 0^\circ$ C and solve for T_a, the ambient (farfield) temperature, L_T, the decay scale, and y_o, the T-rake offset by minimizing $\sum_{n=1}^{8} (T(y_n) - \widehat{T}(y_n))^2$ for each of the n thermistors. T_a and L_T are shown Fig. 4(c); y_o was 5.4, 1.0 & 13 cm for cases 1,2 & 3. The melt-plumes' thermal lengthscales ($L_T = 1 - 4$ cm) are a factor of ten smaller than L_w ($= 20 - 40$ cm); like L_w, L_T is largest during periods of strong crossflow. The consequences of these differences are evident in the mean temperature profile (Fig. 4c and supplement), where two length scales also emerge: one that controls visco-diffusive transports and shapes the inner boundary layer (L_T), and a second that characterizes energetic turbulent transports in the outer boundary layer and diffuses (reduces) larger-scale gradients of T for $y > 10$ cm.

Turbulence: Of relevance to ice melt is the near-boundary TKE, which we compute from along-beam structure functions (Wiles et al., 2006) (Fig. 4d). We employ this technique because it does not depend on relationships between acoustic beams, and hence relaxes assumptions of spatial homogeneity. While TKE is relatively uniform in the strong crossflow (red line), it increases towards the boundary (with a maximum at $\sim$ 10 cm) for both periods when melt-plume velocities dominated the KE. This suggests a different source of TKE in each case: shear production during the strong crossflow vs. buoyancy production when the external flow weakened.

We calculate the horizontal turbulent heat flux as $j_q = \rho c_p K_T dT/dy$ where ρ and c_p are the density and heat capacity of seawater, K_T is the turbulent diffusivity and dT/dy the background temperature gradient. We estimate $K_T \approx \kappa u' \ell$, where $\kappa = 0.4$ is von Karman's coefficient, $u' \approx \sqrt{\text{TKE}}$, and ℓ is the lengthscale of the energy-containing eddies. In analogy to Perlin et al. (2005), we modify the canonical law-of-the wall scaling (for which ℓ is the distance to the boundary) by limiting the characteristic lengthscale far from the boundary to be that of the plume's eddies, which we approximate as $w/(dw/dy)$. Based on these *law-of-the-wall* modifications and using Eckert and Jackson (1950)'s model (equation 1) to estimate plume eddy size, we find $\ell = \max(y, \widehat{w}/(d\widehat{w}/dy))$, which increases linearly ($\ell = y$) for $y < 0.75 L_w$ and then decreases almost linearly to 0 at $\ell = 3.3 L_w$. K_T is found to have similar magnitude and structure for all three cases; j_q is about twice as high for the unsteady plume as the other 2 cases. Note that $j_q = 1$ kW/m^2 is equivalent to 1 cm/hour of ice melt.

Eckert and Jackson (1950)'s formulation also provides a convenient way to compute the vertical stress at the ice boundary

$$\tau_w = 0.0225 \rho w_1^2 \left(\frac{\nu}{w_1 \delta} \right)^{1/4} \tag{4}$$

and has been found consistent with lab and numerical simulations of turbulent flow from a vertically oriented source of distributed buoyancy (Parker et al., 2021; Zhao et al., 2024). We find τ_w which is 0.0098 and 0.0053 Pa for the strong plumes, two to five times larger than $\tau_w = 0.0022$ Pa for the case of a cross-flow. For comparison, the stress associated with the horizontal flow (assuming $\tau_u = \rho C_d u^2$ with $C_d = 2 \times 10^{-3}$) is 0.0072 Pa, similar to that of τ_w in the plumes; τ_u is roughly 30$\times$ smaller during weak crossflow.

6 Interpretation

Much of what we have learned about melt comes from limiting cases of weakly-turbulent laboratory experiments (Josberger & Martin, 1981; McConnochie & Kerr, 2017), idealized numerical modelling (Gayen et al., 2016; Zhao et al., 2024), measurements under horizontal sea ice (McPhee et al., 1987), or inferences from farfield observations (Jackson et al., 2020). A remaining challenge is understanding the connections between outer turbulent scales and molecular transports across a real ice interface, i.e., the exchanges of buoyancy, heat and momentum are fueled by dynamics sketched in Fig. 1A that have until now been largely studied in isolation or under idealized settings.

Our observations of iceberg-scale boundary layers are thicker and more energetic than those simulated in the lab or modelled numerically. Here, rising currents and their turbulence extend 20-50 cm from the ice, contrasting the 1-10 cm lateral scales in simulated flows. And while the strongest temperature anomalies (a proxy for melt buoyancy) are confined within a 1-4 cm e-folding distance from the ice, the heat transport extends far from the boundary. Qualitatively, this is evidenced by the sweeps in T (figure 3), driven by eddies that cyclically advect warm waters toward the boundary and extrude meltwater across the plume on ~ 100 sec timescales. These eddies are responsible for the turbulent heat flux j_q (Fig. 4f).

7 Conclusions

Recent observations of thick meltwater intrusions (Jackson et al., 2020) and unexpectedly high frontal ablation rates (Sutherland et al., 2019) have led to suggestions that Holland and Jenkins (1999) and Jenkins (2011)'s models need to be revisited. Some have suggested transfer coefficients need to be modified (Jackson et al., 2020), others have suggested we need a new empirical model (Schulz et al., 2022), constrained by observations, that is "physically plausible," but not physics based. Neither approach is particularly satisfying because they require arbitrary tuning of coefficients to match observations. The details of the physics are important.

Here we demonstrate the ways in which meltwater buoyancy energizes near-boundary turbulence adjacent to a near-vertical section of an iceberg originating from Xeitl Sít' glacier. Importantly, when external sources of mechanical energy are weak, buoyant convection becomes dominant, driving vertical flows that enhance near-boundary turbulence. While these "meltwater plumes" varied in character, their mean structure was well-described by fits to various powerlaw and exponential functions, and provide a means of quantifying scales of the flow.

While the character of real ambient melt plumes is similar to that predicted by theory (Wells & Worster, 2008), lab (Josberger & Martin, 1981) or numerical simulation (Gayen et al., 2016), the natural flows we observe are significantly more energetic. For example, the sole laboratory study to measure temperature within a turbulent boundary layer adjacent vertical melting ice (Josberger

& Martin, 1981) found turbulent temperature fluctuations to be confined within 2-10 mm of the ice, with fluid outside that layer being quiescent and only occasionally being entrained towards the boundary. In contrast, the boundary layer flows observed here are stronger, broader, and produce higher heat fluxes than these idealized studies.

Our observations confirm that meltwater buoyancy can energize turbulence in the ice-adjacent boundary layer as effectively as a moderate external flow, plausibly driving similar meltrates in both cases. But what sets the TKE, j_q and controls the meltrate? While idealized studies provide some insight and intuition, the feedbacks that control melt cannot be determined from the local dynamics alone. For example, we have shown that a flow – forced ostensibly by the same external conditions – can have dramatically different character (compare Fig. 2 panels a-c with d-f). We hypothesise that the interplay between externally-driven turbulence and meltwater convection is critical to the flow dynamics: both shear and buoyant production influence the coherent structures that are of first order importance of turbulent exchange across this boundary layer. Further direct observations that capture the phenomenology of *real* melt-driven boundary-layers and elucidate the range of dynamical possibilities are critical to inform the next generation of experiments and parameterizations.

8 Open Research

All data are available at the National Snow and Ice Data Center `http://nsidc.org/`

Acknowledgments

This work was funded by the NSF (OPP-2023674) and Keck Foundation. We also thank Bridget Ovall and Lucy Waghorn for providing photographs, and Scott and Julie Hursey and Lila and Grant Trask for support of our field operations in Petersburg Alaska.

References

Bendtsen, J., Rysgaard, S., Carlson, D. F., Meire, L., & Sejr, M. K. (2021). Vertical mixing in stratified fjords near tidewater outlet glaciers along Northwest Greenland. *Journal of Geophysical Research: Oceans*, *126*(8), e2020JC016898.

Carroll, D., Sutherland, D., & Hudson, B. (2016). The impact of glacier geometry on meltwater plume structure and submarine melt in Greenland fjords. *Geophysical Research Letters*, *43*.

Cowton, T., Slater, D., Sole, A., Goldberg, D., & Nienow, P. (2015, feb). Modeling the impact of glacial runoff on fjord circulation and submarine melt rate using a new subgrid-scale parameterization for glacial plumes. *Journal of Geophysical Research: Oceans*, *120*(2), 796–812. Retrieved from `http://doi.wiley.com/10.1002/2014JC010324` doi: 10.1002/2014JC010324

Cusack, J. M., Jackson, R. H., Nash, J. D., Skyllingstad, E., Pettit, E. C., Sutherland, D. A., … Amundson, J. M. (2023). Internal gravity waves generated by subglacial discharge: Implications for tidewater glacier melt. *Geophysical Research Letters*, *50*(12), e2022GL102426.

Eckert, E. R. G., & Jackson, T. W. (1950). Analysis of turbulent free-convection boundary layer on flat plate. *National Advisory Committee on Aeronautics*, *Technical Note 2207*.

Fer, I., McPhee, M. G., & Sirevaag, A. (2004). Conditional statistics of the Reynolds stress in the under-ice boundary layer. *Geophysical Research Letters*, *31*(15).

Gade, H. G. (1979). Melting of ice in sea water: A primitive model with application to the Antarctic ice shelf and icebergs. *Journal of Physical Oceanography*, *9*(1), 189–198.

Gargett, A. E. (1989). Ocean turbulence. *Annual Review of Fluid Mechanics*, *21*(1), 419–451.

Gayen, B., Griffiths, R. W., & Kerr, R. C. (2016, May). Simulation of convection at a vertical ice face dissolving into saline water. *Journal of Fluid Mechanics*, *798*, 284–298.

Holland, D. M., & Jenkins, A. (1999). Modeling thermodynamic ice-ocean interactions at the base of an ice shelf. *Journal of Physical Oceanography*, *29*(8), 1787–1800.

Jackson, R., Nash, J., Kienholz, C., Sutherland, D., Amundson, J., Motyka, R., … Pettit, E. (2020). Meltwater intrusions reveal mechanisms for rapid submarine melt at a tidewater glacier. *Geophysical Research Letters*, *47*(2), e2019GL085335.

Jenkins, A. (2011). Convection-driven melting near the grounding lines of ice shelves and tidewater glaciers. *J. Phys. Oceanogr.*, *41*(12), 2279–2294.

Jenkins, A., Dutrieux, P., Jacobs, S. S., McPhail, S. D., Perrett, J. R., Webb, A. T., & White, D. (2010, jun). Observations beneath Pine Island Glacier in West Antarctica and implications for its retreat. *Nat. Geosci.*, *3*(7), 468–472. Retrieved from `http://www.nature.com/doifinder/10.1038/ngeo890` doi: 10.1038/ngeo890

Josberger, E. G., & Martin, S. (1981). A laboratory and theoretical study of the boundary layer adjacent to a vertical melting ice wall in salt water. *Journal of Fluid Mechanics*, *111*, 439–473.

Kerr, R. C., & McConnochie, C. D. (2015, January). Dissolution of a vertical solid surface by turbulent compositional convection. *Journal of Fluid Mechanics*, *765*, 211–228.

Kimura, S., Holland, P. R., Jenkins, A., & Piggott, M. (2014). The effect of meltwater plumes on the melting of a vertical glacier face. *Journal of Physical Oceanography*, *44*, 3099–3117.

Kline, S. J., Reynolds, W. C., Schraub, F., & Runstadler, P. (1967). The structure of turbulent boundary layers. *Journal of Fluid Mechanics*, *30*(4), 741–773.

MacAyeal, D. R. (1985). Evolution of tidally triggered meltwater plumes below ice shelves. *Oceanology of the Antarctic Continental Shelf*, 133–143.

Macias, J., Bante-Guerra, J., Cervantes-Alvarez, F., Rodrìguez-Gattorno, G., Arés-Muzio, O., Romero-Paredes, H., ... others (2019). Thermal characterization of carbon fiber-reinforced carbon composites. *Applied Composite Materials*, *26*, 321–337.

Magorrian, S. J., & Wells, A. J. (2016). Turbulent plumes from a glacier terminus melting in a stratified ocean. *Journal of Geophysical Research: Oceans*, *121*(7), 4670–4696.

McConnochie, C. D., & Kerr, R. C. (2017, July). Testing a common ice-ocean parameterization with laboratory experiments. *Journal of Geophysical Research Oceans*, *122*(7), 5905–5915.

McPhee, M. G., Maykut, G. A., & Morison, J. H. (1987). Dynamics and thermodynamics of the ice/upper ocean system in the marginal ice zone of the Greenland Sea. *Journal of Geophysical Research*, *92*(C7), 7017–7031.

Parker, D., Burridge, H., Partridge, J., & Linden, P. (2021). Vertically distributed wall sources of buoyancy. Part 1. Unconfined. *Journal of Fluid Mechanics*, *907*, A15.

Perlin, A., Moum, J., Klymak, J., Levine, M., Boyd, T., & Kosro, P. (2005). A modified law-of-the-wall to describe velocity profiles in the bottom boundary layer. *J. Geophys. Res.*, *110*(C10S10). (doi:10.1029/2004JC002310)

Schulz, K., Nguyen, A., & Pillar, H. (2022). An improved and observationally-constrained melt rate parameterization for vertical ice fronts of marine terminating glaciers. *Geophysical Research Letters*, *49*(18), e2022GL100654.

Slater, D., Goldberg, D. N., Nienow, P. W., & Cowton, T. R. (2016). Scalings for submarine melting at tidewater glaciers from buoyant plume theory. *Journal of Physical Oceanography*, *46*, 1839–1855.

Smith, R. R. (1972). *Characteristics of turbulence in free convection flow past a vertical plate.* (Unpublished doctoral dissertation). Queen Mary University of London.

Smyth, W. D. (1999). Dissipation-range geometry and scalar spectra in sheared stratified turbulence. *J. Fluid Mech.*, *401*, 209–242.

Stanton, T. P., Shaw, W., Truffer, M., Corr, H., Peters, L., Riverman, K., … Anandakrishnan, S. (2013). Channelized ice melting in the ocean boundary layer beneath Pine Island Glacier, Antarctica. *Science*, *341*(6151), 1236–1239.

Sutherland, D., Jackson, R. H., Kienholz, C., Amundson, J. M., Dryer, W., Duncan, D., … Nash, J. (2019). Direct observations of submarine melt and subsurface geometry at a tidewater glacier. *Science*, *365*(6451), 369–374.

Thomson, J., Schwendeman, M. S., Zippel, S. F., Moghimi, S., Gemmrich, J., & Rogers, W. E. (2016). Wave-breaking turbulence in the ocean surface layer. *Journal of Physical Oceanography*, *46*(6), 1857–1870.

Tsuji, T., & Nagano, Y. (1988). Characteristics of a turbulent natural convection boundary layer along a vertical flat plate. *International journal of heat and mass transfer*, *31*(8), 1723–1734.

Watkins, R. H., Bassis, J. N., & Thouless, M. (2021). Roughness of ice shelves is correlated with basal melt rates. *Geophysical Research Letters*, *48*(21), e2021GL094743.

Weiss, K., Nash, J., Wengrove, M., & Others. (2024). Direct measure of melt at an iceberg. *Geophys. Res. Lett.*, *in prep*(0), 00-00.

Wells, A. J., & Worster, M. G. (2008). A geophysical-scale model of vertical natural convection boundary layers. *Journal of Fluid Mechanics*, *609*, 111–137.

Wengrove, M. E., Pettit, E. C., Nash, J. D., Jackson, R. H., & Skyllingstad, E. D. (2023). Melting of glacier ice enhanced by bursting air bubbles. *Nature Geoscience*, *16*(10), 871–876.

Wiles, P., Rippeth, T., Simpson, J., & Hendricks, P. (2006). A novel technique for measuring the rate of turbulent dissipation in the marine environment. *Geophys. Res. Lett.*, *33*(21), L21608.

Xu, Y., Rignot, E., Fenty, I., Menemenlis, D., & Flexas, M. M. (2013). Subaqueous melting of Store Glacier, west Greenland from three-dimensional, high-resolution numerical modeling and ocean observations. *Geophysical Research Letters*, *40*(17), 4648–4653.

Zhao, K., Skyllingstad, E., & Nash, J. (2024). Improved parameterizations of vertical ice-ocean boundary layers and melt rates. *Gephys. Res. Lett*, *in press*.

Zhao, K., Stewart, A., McWilliams, J., Fenty, I., & Rignot, E. (2023). Standing eddies in glacial fjords and their role in fjord circulation and melt. *Journal of Physical Oceanography*, *53*(3), 821–840.

Turbulent Dynamics of Buoyant Melt Plumes Adjacent Near-Vertical Glacier Ice

Jonathan D Nash[1], Kaelan Weiss[1], Meagan E Wengrove[1], Noah Osman[1], Erin C Pettit[1], Ken Zhao[1,2], Rebecca H Jackson[3], Jasmine Nahorniak[1], Kyle Jensen[1], Erica Tindal[1], Eric D Skyllingstad[1], Nadia Cohen[1] and David Sutherland[4]

[1]Oregon State University
[2]University of Southern California, San Diego
[3]Rutgers University
[4]University of Oregon

Key Points:

- Robotic observations at a submerged near-vertical iceberg face capture turbulent dynamics of buoyant melt plumes and background currents
- Buoyant plumes extend 20-50 cm from the boundary, undulate on 100-s periods, and drive horizontal turbulent transports.
- Buoyant plumes can be more effective than horizontal flows in energizing boundary layer turbulence and heat flux.

Corresponding author: Jonathan D. Nash, `Jonathan.Nash+GRL@oregonstate.edu`

Abstract

At marine-terminating glaciers, the interplay between meltwater buoyancy and local currents control turbulent exchanges. Because of challenges in making centimeter-scale measurements at glaciers, turbulent dynamics at near-vertical ice-ocean boundaries are poorly constrained. Here we present the first observations from instruments robotically-bolted to an underwater ice face, and use these to elucidate the tug-of-war between meltwater-derived buoyancy and externally-forced currents in controlling boundary-layer dynamics. Our observations captured two limiting cases of the flow. When external currents are weak, meltwater buoyancy energizes the turbulence and dominates the near-boundary stress. When external currents strengthened, the plume diffused far from the boundary and the associated turbulence decreases. As a result, even relatively weak buoyant melt plumes are as effective as moderate shear flows in delivering heat to the ice. These are the first *in-situ* observations to demonstrate how buoyant melt plumes energize near-boundary turbulence, and why their dynamics are critical in predicting ice melt.

Plain Language Summary

Melting glaciers are projected to produce several inches of sea level rise over the next few decades. Despite this threat, the fundamental fluid dynamics which drive melt at tidewater glaciers remain poorly characterized. This is primarily attributed to challenges associated with measuring the temperature and velocity of ocean water at the submerged cliffs of actively calving glaciers. To this end, we have developed a robotically-deployed instrument that can be bolted to a glacier's face. This instrument is capable of measuring temperature and kinetic energy of ocean waters within a few inches of the ice, representing the first measurements of their kind. Our observations demonstrate the ways in which meltwater at ice boundaries can accelerate melt. In particular, the meltwater tends to be less salty (and hence lighter) than the nearby ocean waters (which are salty, warm and heavy), so the meltwater rises along the ice face, creating an energetic, near boundary flow. With our new measurements, we show that these flows are as important as large-scale currents in providing energy to the ice to fuel melt. We anticipate these data will help our community create more accurate models of ice melt needed to predict the advance or retreat of marine ice cliffs of Greenland, Alaska and Antarctica.

1 Introduction

Directly quantifying the rate of ice-melt at the near-vertical cliffs of marine-terminating glaciers is a challenge due to the boundary's inaccessibility to traditional forms of sampling. The ice melt-process is also complicated because the thermodynamics depend on how local buoyancy production (from melt) combines with the external forcing (temperature T, salinity s, velocity $\vec{u}$) to control energy flow across the ice boundary. The heat flux j_q, for example, is ultimately set by strong thermal gradients near the diffusive scales, which provides buoyant energy that fuels the turbulent energy cascade. In turn this cascade also intensifies the near-boundary thermal gradients that drive melt and supply buoyant energy (Fig. 1A). This feedback loop is at odds with traditional turbulence theory that often assumes isotropy, homogeneity and the ability to separate the spatial scales of energy sources (large) and sinks (small).

At an ice face, we hypothesize that meltwater detaches from the boundary in fine-scale turbulent sweeps, similar to those observed under sea ice (Fer et al., 2004) and in atmospheric boundary layers (Kline et al., 1967), but here producing buoyant energy at the same small scales that dominate viscous dissipation. Meltwater buoyancy thus injects additional momentum at very small scales – near the viscous tail of a downscale turbulent energy cascade likely fueled both by the large-scale buoyant forcing (Xu et al., 2013) alongside a zoo of classic ocean- (Gargett, 1989) and fjord-specific (Bendtsen et al., 2021) turbulence sources. Further complicating the dynamics are the energy exchanges as parcels entrain buoyancy from the background stratification as they move vertically against gravity, which can represent either a source or sink of energy (Magorrian & Wells, 2016; Kimura et al., 2014).

Beneath gently-sloping, near-horizontal ice-ocean interfaces, meltwater buoyancy drives along-ice flow. However, this buoyancy also provides static stability, so turbulent exchanges primarily occur through hydrodynamic instability such as Kelvin-Helmholz billows (Smyth, 1999). In 1984, a comprehensive set of observations of turbulent melt dynamics in the Marginal Ice Zone of the Greenland Sea were acquired (McPhee et al., 1987). McPhee et al. (1987) used these data to create an empirical model to predict melt from T, s, and the turbulent stress τ, which formed the basis for the canonical three-equation melt parameterization (Holland & Jenkins, 1999). Because the stability of the ice permitted detailed, high-accuracy measurements to be obtained, this parameterization (based on ice-melt thermodynamics and three empirical coefficients derived from those experiments), remains the community's primary and only way to predict melt beneath ice shelves (Jenkins et al., 2010) if the relevant flow ($\vec{u}$, T and s) can be prescribed.

As the ice interface approaches vertical, meltwater can generate sufficient buoyancy to become convectively unstable and directly energize turbulence, as demonstrated in the laboratory by Josberger and Martin (1981). Because the entrainment of warm ocean water increases with plume strength, the melt process creates a positive feedback (Fig. 1A) that further energizes the plume to enhance melt. Eckert and Jackson (1950) created a framework for characterizing turbulent free-convection boundary layers adjacent to a heated plate (for air at $Pr = 1$), and their study remains highly relevant today (Parker et al., 2021). However, the ice-melt problem is more complex because: (1) turbulence is generated by both buoyant convection and shear production (Josberger & Martin, 1981; Zhao et al., 2024); (2) melt can be driven by both salinity or thermal gradients, each which diffuse and influence density in different ways (Gade, 1979; Kerr & McConnochie, 2015); (3) vertical gradients of ocean properties (such as density) affect buoyancy production of turbulent energy and the growth of turbulent plumes (i.e., Magorrian and Wells (2016)); and (4) in addition to buoyancy, other sources of velocity like internal waves (Cusack et al., 2023) or mean currents (Jackson et al., 2020; Zhao et al., 2023) affect shear production of turbulent energy.

Theoretical models (i.e. Wells and Worster (2008)) provide a framework to describe plume evolution, but still require turbulence closure derived from laboratory experiments (McConnochie & Kerr, 2017), numerical experiments (Gayen et al., 2016), or observational analogies (McPhee et al., 1987). At the geophysical scale, empirical models have been developed that assume simplified geometries and turbulence closure. For example, Jenkins (2011) used the framework of MacAyeal (1985) to couple buoyant plume theory with the 3-equation melt model (McPhee et al., 1987) to predict the downstream flow evolution. By prescribing an idealized plume geometry, this framework has been used to predict the freshwater distribution from a localized subglacial discharge (Cowton et al., 2015; Carroll et al., 2016) and also for distributed melt (Magorrian & Wells, 2016; Jackson et al., 2020).

To date, there are no experiments analogous to the 1984 sea-ice observations (McPhee et al., 1987) that could be used to constrain the flow and meltrate parameterization for a vertical ice face. In addition to uncertainty in values of drag and transfer coefficients, there is also debate about how to formulate the coupled models themselves. Part of this debate stems from observations of glacier face ablation (Sutherland et al., 2019) and the existence of large-scale meltwater intrusions (Jackson et al., 2020) that imply significantly higher meltrates than predicted with the above theories as applied in their commonly-used forms. It has been suggested that the boundary layers are energized by external currents which increases the turbulent transfer coefficients;

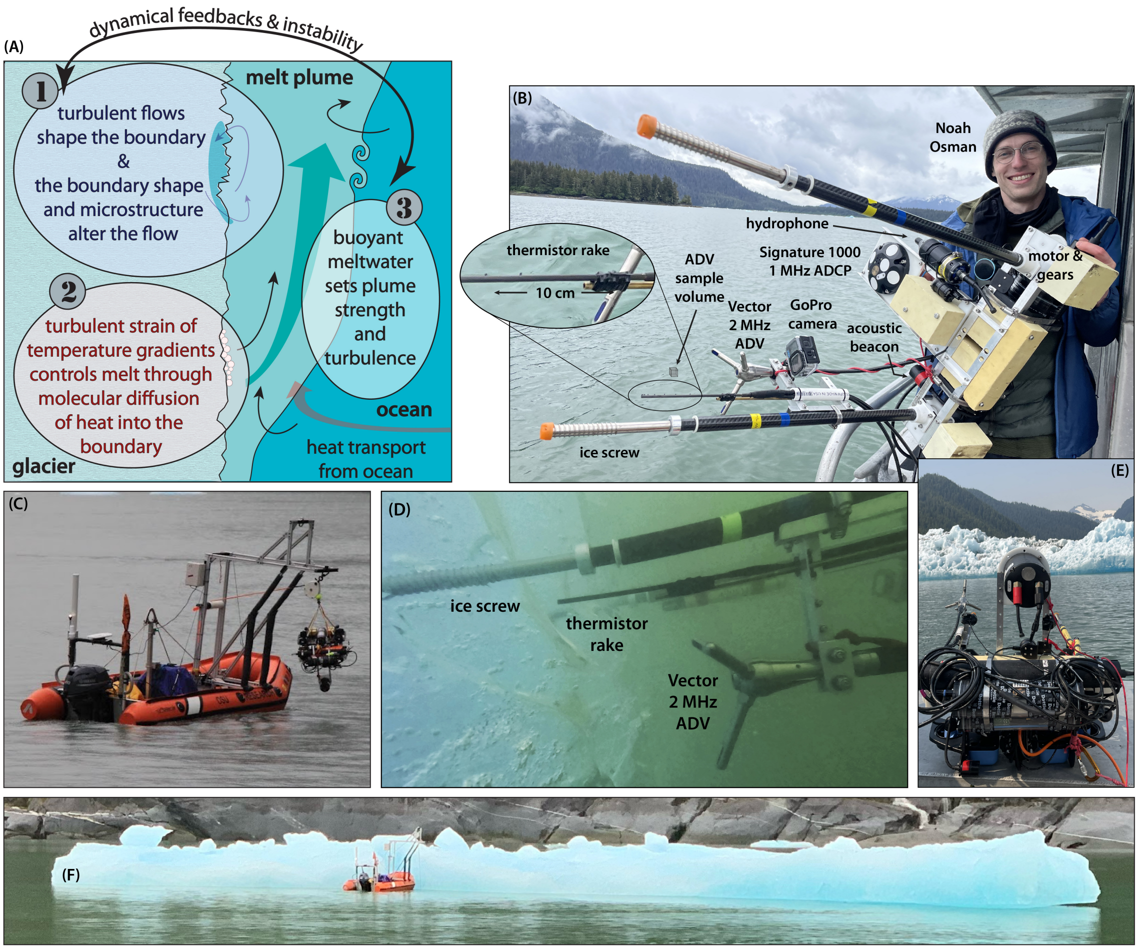

Figure 1. (A) Cartoon illustrates the interplay between (1) ice morphology (2) turbulent and molecular transports across the ocean-ice interface, and (3) melt-driven buoyant plumes that energize the boundary layer. (B) Meltstake sensors are configured to measure these dynamics with minimal disturbance to the flow. (C) Remotely-operated vessel and winched ROV. (D) Meltstake as deployed 12:40 29 May showing ice structure and the sensors' proximity to the interface; the ADCP is outside the frame of view. (E) A Meltstake riding atop the delivery ROV on deck; iceberg from Xeitl Sít' in background. (F) Remote deployment in progress.

anecdotal evidence suggests this is not unreasonable, i.e., Cusack et al. (2023); Slater et al. (2016); Jackson et al. (2020). Other factors – like energy from exploding air bubbles observed in the lab (Wengrove et al., 2023), or ice roughness and channelization observed beneath ice shelves (Stanton et al., 2013; Watkins et al., 2021) – may also be at play here. It is the purpose of this note to describe the first detailed observations of the turbulent flow at a near-vertical glacier-ice face, and to demonstrate how plume buoyancy and external velocities contribute to melt-dynamics. A concurrent paper (Weiss et al, in prep) will extend the analysis of these data to quantify melt rates and assess bias and uncertainty in current melt parameterizations.

2 Methods

2.1 The Glacier Meltstake

The Meltstake is a submarine device (Fig. 1B-F) that is remotely bolted to a near-vertical glacier-ice face to directly measure melt and the spatial structure of near-boundary velocity, temperature and turbulence. It is called a “Meltstake” in analogy to the subaerial ablation stakes used by glaciologists to measure ice accumulation and ablation in the field. It is designed to be a stable platform to observe the flow in a reference frame fixed to the ice and in ways that minimize the system’s thermal and hydrodynamic impact on melt dynamics.

The body of the Meltstake is suspended outward from the ice on two, 61-cm long carbon fiber tubes, chosen for their mechanical stiffness and low thermal conductivity $5 \times 10^{-6}\mathrm{m}^2/\mathrm{s}$ (Macias et al., 2019). Ice screws mounted on the ends of these 16-mm diameter tubes turn using Blue Robotics T200 motors at 23:1 reduction. Each screw-assembly rotates within a 25-mm carbon sheath to allow instruments to be rigidly attached at various distances from the ice. A Raspberry Pi “brain” controls drilling power, schedule and underwater communications with a remotely-operated vehicle (ROV) through a long-range 28 kHz Delphis Subsea modem.

The Meltstake is transported to the ice face using a BlueRobotics ROV, equipped with a Ping360 imaging sonar and video camera for underwater navigation. The Meltstake is pinned to the ROV and held in place with a Newton linear actuator. The ROV can be deployed from either a robotic vessel equipped with a remotely-operated winch or a traditional vessel. High-power Ubiquiti Rocket WiFi allows remote operation of the ROV/Meltstake from several kms away using the standard QGroundControl software. Acoustic messages sent from the ROV trigger drill operations. Once the the Meltstake “bites” into the ice, the ROV releases from it. The freed ROV can then monitor the meltstake, request further manual drilling, update the Meltstake’s autonomous schedule, or request its release to return to the surface. The unit is rated to 100-m depths, ballasted 10 N buoyant, and has a flasher and GPS/satellite beacon for recovery.

2.2 Experimental setting and measurements

Boundary-layer measurements were made at a freely-floating iceberg with 10-m draft, $\sim$20 km down-fjord from Xeitl Sít’(also called LeConte Glacier) in Southeast Alaska. We deployed the Meltstake on a vertical face of the ice at 6.5-m depth starting at 20:40 UTC, May 29, 2023. As the iceberg melted, we sent acoustic “drill” commands (at 21:39 and 23:05) to advance the Meltstake and move sensors closer to the ice interface. At 23:48 it was released and recovered.

At 00:46, May 30 it was again delivered to the same iceberg at 8.5-m depth, drilled further at 01:46, and released at 02:20.

Velocity was imaged with a 5-beam Nortek 1000 kHz Acoustic Doppler Current Profiler (ADCP) in pulse-coherent mode (4 Hz sampling with 3-4 cm bins). Because of high acoustic backscatter from ice, ADCP data are contaminated by spurious reflections from sidelobes at ranges that exceed the distance of the closest transducer-to-ice distance. We thus attempted to orient the ADCP so that the 4 slant beams encounter the ice at approximately the same range. We use a right-hand coordinate system in which x is along-ice, y is horizontal and positive away from the ice, and z is up. ADCP data were recorded in along-beam coordinates and used for two purposes: (1) opposing beams were combined to determine the bulk vertical (w) and along-ice (u) velocity over the 10-70 cm footprint of the spreading beams; (2) along-beam velocities were used to compute (i) the velocity v from the central beam and (ii) turbulent statistics of the flow using the structure function method of Wiles et al. (2006) as implemented by Thomson et al. (2016). Echo backscatter from a Nortek Vector Acoustic Doppler Velocimeter was used to determine meltrate.

Near-boundary temperature was measured using a thermistor “T-rake,” a horizontal array of eight, fast-response thermistors, each exposed downward into the expected flow at distances of 2, 4, 7, 12, 23, 39, 58 and 84 mm from the tip of a carbon tube (Fig. 1B, S1 and supplement). Three fast-response RBR Solos provided additional temperature measurements at 10, 35 and 60 cm from the ice. Salinity was obtained from nearby vertical profiles using a RBR Concerto CTD and ranged from 27.4-28.4 within the $\pm$1-m depth range around each deploment.

3 Observations of buoyancy- and externally-forced boundary layers

Here we examine three time periods that illustrate the range of flow patterns observed (Fig. 2). The first two cases represent a boundary layer energized by the vertical rise of buoyant meltwater, which we term “buoyancy-forced.” The third is an example we term “externally-forced,” because horizontal velocities were significantly stronger than those of the vertically-rising flows.

Case 1A: Quasi-steady buoyant plume. Shortly after the Meltstake was deployed (at 6.5 m depth, and under weak, $u \sim 1$ cm/s, crossflow conditions), a quasi-steady plume was observed to flow vertically up the ice at 2-4 cm/s within $\sim$ 20 cm of the ice (Fig. 2a-c). During this time, the strongest temperature anomalies (indicative of melt waters) were only observed by sensors within a few millimeters of the T-rake tip, and $\sim$5 cm from the ice.

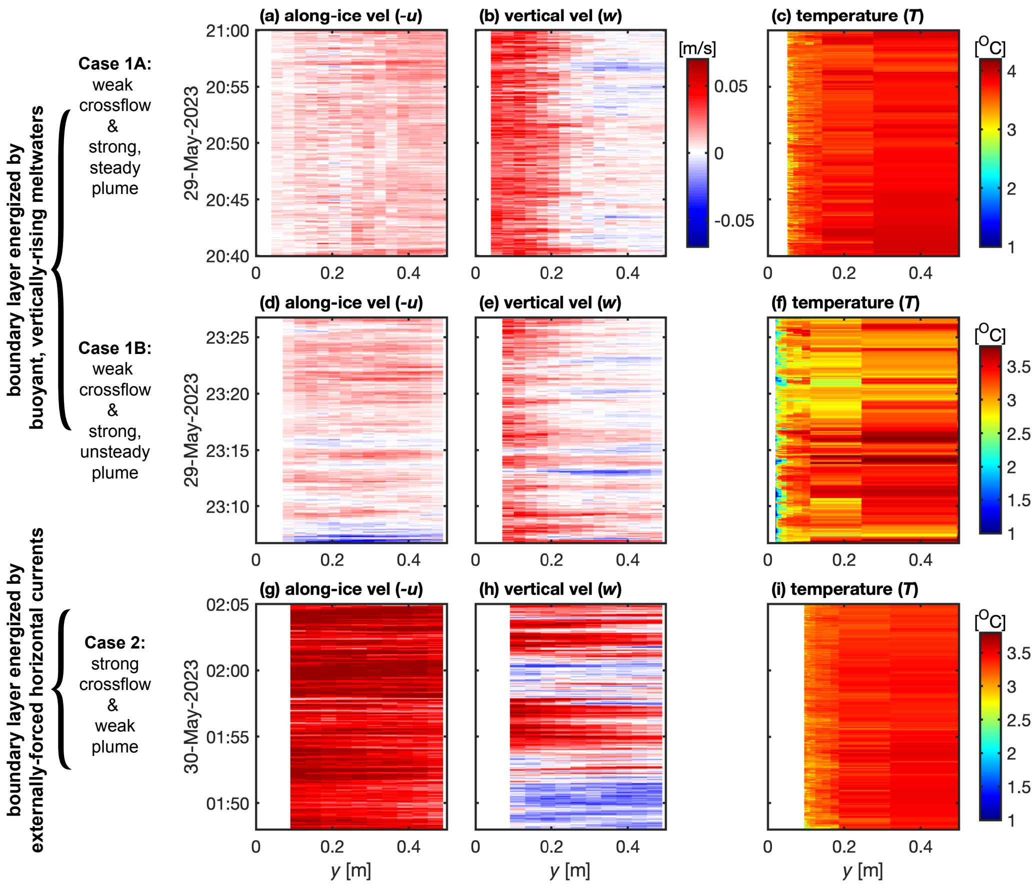

Figure 2. Horizontal, along-ice velocity (a,d,g), vertical velocity (b,e,h), and temperature (c,f,i) within 0.5 m of the ice interface for three twenty-minute periods. Between Case 1A and 1B (at 6.5 m depth), the Meltstake was advanced 6 cm further into the ice, placing the thermistor rake within 2 cm of the ice, but also increasing ADCP sidelobe contamination; Case 2 was a separate deployment at 8.5 m depth. Distance from ice (y) was computed acoustically for $-u$ and w (Weiss et al., 2024) and using equation 3 to determine y_o for $\widehat{T}$; note that the ice melted 3-5 mm during each 20-min period (Weiss et al., 2024), so we treat y independent of time for these plots.

Case 1B: Strongly-undulating buoyant plume. As time evolved the buoyant plume became more variable in time, weakened in magnitude, and decreased in thickness (Fig. 2d-f). The crossflow also became slightly unsteady (but still weak), undulating with similar timescales as the vertical plume. The Meltstake was also advanced towards the ice between 1A and 1B, yielding T observations within 2 cm from the ice. Temperatures most distant from the ice were observed to increase slightly, and pulses of low-temperature waters were swept 2-10 centimeters from the ice, contrasting the weaker thermal anomalies in case 1A. Far from the boundary ($y > 10$ cm), w alternates sign on ~ 100 second intervals; these pulses appear correlated with temperature. For example, between 23:14 and 23:18 there are several strong vertical velocity reversals that coincide with warm pulses, which could be interpreted as turbulent eddies drawing warm ambient fluid towards the boundary.

Case 2: Strong crossflow. After the Meltstake was released and re-drilled into the ice at 8.5-m depth, the iceberg had moved and tidal flows strengthened, exposing the ice to stronger currents (Fig. 2g-i). At this time, $-u$ averaged 6 cm/s, w was highly variable but upward ($\sim 1{-}1.5$ cm/s) on average, and both undulated with O(5 min) period; $-u$ and w are correlated and somewhat out-of-phase (the weakest w generally correspond to the largest $-u$). Temperature anomalies (indicating the presence of meltwater) were observed close to the boundary.

4 Character of turbulence in the buoyant plume

To glean insight into turbulent dynamics energized by meltwater buoyancy, we examine the undulating plume case (Case 1B) in more detail. We focus on the 5-10 minutes following drilling (at 23:05) and we look in detail at the 11 individual thermistors in the context of the near-boundary velocities (Fig. 3). During the first 5 minutes, the T-rake was in closest proximity to the ice (see supplement), such that the innermost thermistor (2 mm from the T-rake tip; midnight blue in Fig. 3a) was on average 4 mm from the ice.

These temperature data demonstrate a turbulent melt-and-extrude cycle, whereby the first phase of the eddy draws warm water toward the boundary to initiate melt, and the second phase sweeps the cold meltwaters away from the ice. This pattern can be seen in the traces in Fig. 3a: at times when T rises at the outer sensors, temperatures at the inner sensors cool. For example, at 23:11, 23:14 and 23:16, the 3 outer sensors (red traces in Fig. 3a) warm together, while the inner five sensors (blue-green traces) cool in unison. These cold pulses – which reached as low as $0°$ C at times – are the signatures of melt emerging from the boundary. Following these (i.e., at

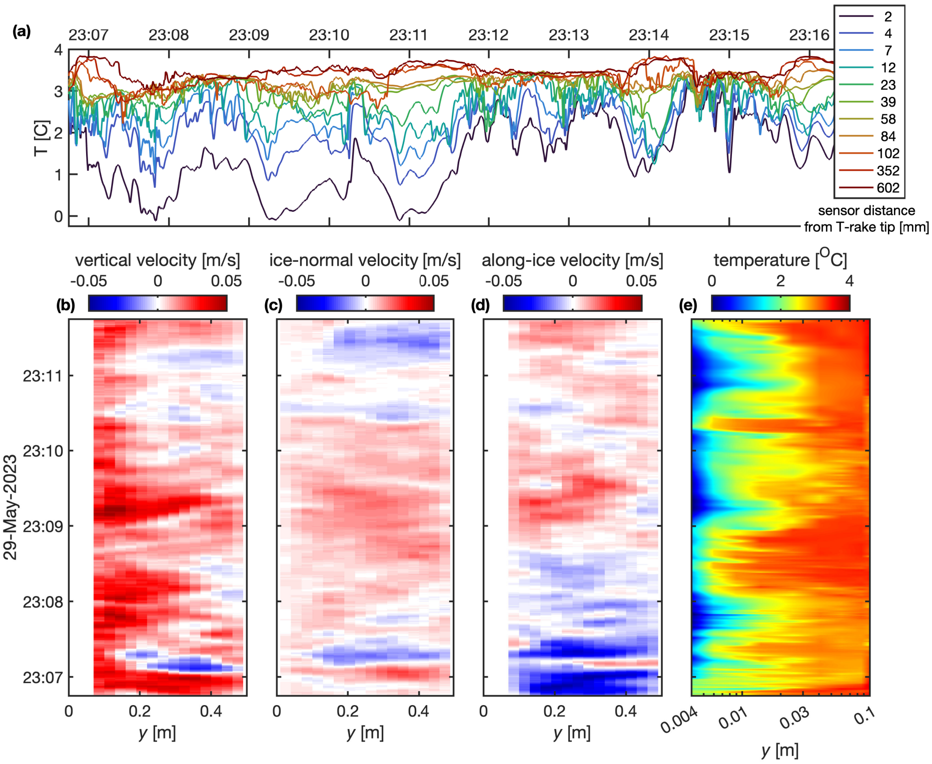

Figure 3. Details of the boundary-layer layer illustrate the dynamics of the unsteady plume: (a) Ten-minute segment of temperature data from the 11 sensors used in Fig. 2f. Lower panels show a zoom-in on the first five minutes of that record on May 29, 2023: (b) vertical velocity, (c) ice-normal velocity (positive/red is away from the ice), (c) along-ice velocity, and (d) temperature, plotted against logarithmic distance coordinates to highlight the smallest scales near the ice boundary. In (c), v is from the ADCP center beam so is least-contaminated by acoustic sidelobes and provides unbiased data almost to the ice surface.

23:12) are periods in which the temperature of all sensors coalesce together, and are the times when warm waters make their closest contact to the ice, presumably temporarily enhance melt.

Anomalies exceeding ~ 1.5 °C (below ambient T_a) were detected 25 mm from the boundary, and coherent across all sensors, indicating a pathway for meltwater to be swept out from the laminar sublayer into the outer layer by turbulence. During these events, the ice-perpendicular velocity (Fig. 3c) was directed away from the face at approximately 1 cm/s, extended 10s of cm from boundary, and varied coherently in all three velocity components. This cycle of perturbations – that brings warm water towards the ice and extrudes cold meltwaters away from the boundary – undulates on 100-s periods, and is the signature of a horizontal eddy-transport of heat that fuels melt.

5 Quantitative differences in flow patterns

To compare the flow characteristics during each of the example time periods, we compute mean profiles of the near-boundary velocity, temperature, turbulent energy and heat transport (Fig. 4). Fits of w and T to empirical functions are used to determine spatial scales, magnitudes and gradients, which we use to determine τ and j_q, both of which are important parameters to predict melt. Consistency between direct turbulence observations and τ derived from Eckert and Jackson (1950)'s self-similar profiles provides confidence in our interpretations.

Velocity: For a convection flow driven by buoyancy from a heated vertical plate, Eckert and Jackson (1950) derived similarity solutions for a Prandtl number ($Pr = 1$) flow. They find the vertical velocity $\widehat{w}$

$$\widehat{w}(\hat{y}) = w_1 \hat{y}^{1/7}(1-\hat{y})^4. \tag{1}$$

is a function of the nondimensional distance from the wall $\hat{y} = y/\delta$, where δ is assumed to vary slowly in z and represents the distance over which the solution is valid ($\widehat{w} \geq 0$); w_1 is a constant. We use this form to characterize the observed plumes' vertical velocity $w(y)$ by minimizing $\sum (w(y) - \widehat{w}(y))^2$ to determine w_1 and δ over 20-minute durations. For this solution, the peak velocity is $w_{max} = 0.5372 w_1$ and the plume width, defined by $\widehat{w}(L_w)/w_{max} = 1/e$ is $L_w = 0.304\delta$. As shown in Fig. 4(b), these fits represent the data well in the region we have observations, and indicate a factor-of-two increase in plume width ($L_w = 44$ cm) during periods of strong crossflow compared to that during weak ($L_w = 21 - 22$ cm). Because w_{max} decreased for large L_w, the total vertical transport, $Q_{plume} = \int_0^\delta \widehat{w} dy = 0.146 w_1 \delta$ was observed to be similar for each of the three cases: 76, 56 and 78 cm^2/s.

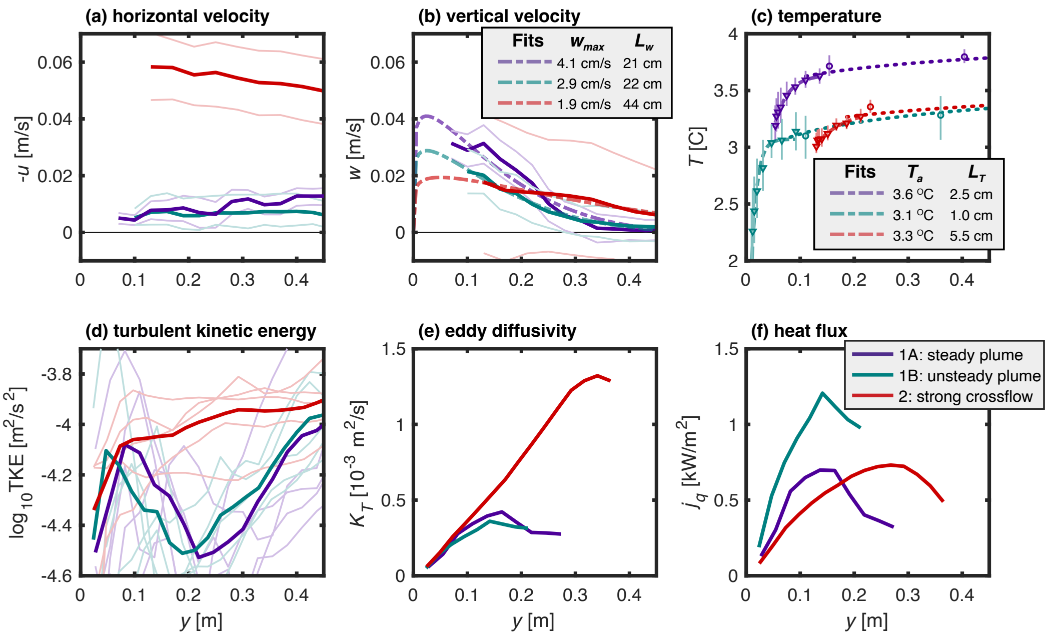

Figure 4. Mean and turbulent characteristics of the observed boundary layers: (a) along-ice velocity $-u$, (b) vertical velocity w, (c) temperature T, (d) turbulent kinetic energy TKE, (e) turbulent diffusivity K_T, and (f) heat flux J_q. Each colored line represents a 20-minute average over the time periods shown in Fig. 2: steady plume (1A, purple), undulating plume (1B, turquoise), strong crossflow (2, red). Thin/light lines in (a-c) define the central 50% of the data. Gaps in (c) separate data from the temperature rake and RBR Solos (separated horizontally by 60 cm and hence responsible for offsets in T). Light dashed lines in (b) and (c) represent eqns. 1, 3 with least-square-fit coefficients as indicated; in (c) fits to eq. 3 use the T-rake data (shown in thick dashed lines) and fits to eq. 2 use the outer 5 T sensors (thin dashed lines). In (d), semi-transparent lines represent estimates of TKE from each of the 5 individual ADCP beams (heavy lines are the means).

Temperature: T-rake timeseries provide temperature and its gradient with sub-centimeter resolution and at close proximity to the ice boundary. Here we use these and Solo data to characterize the thermal boundary layer (see Supplement for details), which we separate into an outer and inner layer.

We begin by considering Eckert and Jackson (1950)'s similarity solution, for which the characteristic lengthscale for $T(y)$ and $w(y)$ assumed the same (δ). In their form (applicable to air ($Pr = 0.7$) and requiring $T = 0$ at the boundary), a substantial temperature gradient (O$\sim$1C/m) is predicted far from the boundary, which is not observed here (Fig. S2). Here we modify their form by introducing ΔT to allow for a lesser temperature drop (relative to ambient T_a) in the outer layer:

$$T = T_a - \Delta T(1 - (y/\delta)^{1/7}). \tag{2}$$

Fits to the outer 5 temperature measurements are roughly consistent with both this form and the logarithmic scaling presented by Tsuji and Nagano (1988) (see Supplement), yeilding a 0.2-0.3 $^\circ$C drop in the outer boundary layer.

Close to the ice, the observed $T(y)$ is inconsistent with (Eckert & Jackson, 1950) eq. (2). Motivated by the early work of Smith (1972) and Tsuji and Nagano (1988), we consider an inner layer shaped by molecular transports and having a different characteristic lengthscale L_T, and arbitrarily assume the following exponential form:

$$\widehat{T}(y) = T_a - (T_a - T_i)e^{-y/L_T}. \tag{3}$$

Here we assume the ice temperature $T_i = 0^\circ$ C and solve for T_a, the ambient (farfield) temperature, L_T, the decay scale, and y_o, the T-rake offset by minimizing $\sum_{n=1}^{8}(T(y_n) - \widehat{T}(y_n))^2$ for each of the n thermistors. T_a and L_T are shown Fig. 4(c); y_o was 5.4, 1.0 & 13 cm for cases 1,2 & 3. The melt-plumes' thermal lengthscales ($L_T = 1 - 4$ cm) are a factor of ten smaller than L_w ($= 20 - 40$ cm); like L_w, L_T is largest during periods of strong crossflow. The consequences of these differences are evident in the mean temperature profile (Fig. 4c and supplement), where two length scales also emerge: one that controls visco-diffusive transports and shapes the inner boundary layer (L_T), and a second that characterizes energetic turbulent transports in the outer boundary layer and diffuses (reduces) larger-scale gradients of T for $y > 10$ cm.

Turbulence: Of relevance to ice melt is the near-boundary TKE, which we compute from along-beam structure functions (Wiles et al., 2006) (Fig. 4d). We employ this technique because it does not depend on relationships between acoustic beams, and hence relaxes assumptions of spatial homogeneity. While TKE is relatively uniform in the strong crossflow (red line), it increases towards the boundary (with a maximum at $\sim$ 10 cm) for both periods when melt-plume velocities dominated the KE. This suggests a different source of TKE in each case: shear production during the strong crossflow vs. buoyancy production when the external flow weakened.

We calculate the horizontal turbulent heat flux as $j_q = \rho c_p K_T dT/dy$ where ρ and c_p are the density and heat capacity of seawater, K_T is the turbulent diffusivity and dT/dy the background temperature gradient. We estimate $K_T \approx \kappa u' \ell$, where $\kappa = 0.4$ is von Karman's coefficient, $u' \approx \sqrt{\text{TKE}}$, and ℓ is the lengthscale of the energy-containing eddies. In analogy to Perlin et al. (2005), we modify the canonical law-of-the wall scaling (for which ℓ is the distance to the boundary) by limiting the characteristic lengthscale far from the boundary to be that of the plume's eddies, which we approximate as $w/(dw/dy)$. Based on these *law-of-the-wall* modifications and using Eckert and Jackson (1950)'s model (equation 1) to estimate plume eddy size, we find $\ell = \max(y, \widehat{w}/(d\widehat{w}/dy))$, which increases linearly ($\ell = y$) for $y < 0.75L_w$ and then decreases almost linearly to 0 at $\ell = 3.3L_w$. K_T is found to have similar magnitude and structure for all three cases; j_q is about twice as high for the unsteady plume as the other 2 cases. Note that $j_q = 1$ kW/m^2 is equivalent to 1 cm/hour of ice melt.

Eckert and Jackson (1950)'s formulation also provides a convenient way to compute the vertical stress at the ice boundary

$$\tau_w = 0.0225 \rho w_1^2 \left(\frac{\nu}{w_1 \delta} \right)^{1/4} \tag{4}$$

and has been found consistent with lab and numerical simulations of turbulent flow from a vertically oriented source of distributed buoyancy (Parker et al., 2021; Zhao et al., 2024). We find τ_w which is 0.0098 and 0.0053 Pa for the strong plumes, two to five times larger than $\tau_w = 0.0022$ Pa for the case of a cross-flow. For comparison, the stress associated with the horizontal flow (assuming $\tau_u = \rho C_d u^2$ with $C_d = 2 \times 10^{-3}$) is 0.0072 Pa, similar to that of τ_w in the plumes; τ_u is roughly 30$\times$ smaller during weak crossflow.

6 Interpretation

Much of what we have learned about melt comes from limiting cases of weakly-turbulent laboratory experiments (Josberger & Martin, 1981; McConnochie & Kerr, 2017), idealized numerical modelling (Gayen et al., 2016; Zhao et al., 2024), measurements under horizontal sea ice (McPhee et al., 1987), or inferences from farfield observations (Jackson et al., 2020). A remaining challenge is understanding the connections between outer turbulent scales and molecular transports across a real ice interface, i.e., the exchanges of buoyancy, heat and momentum are fueled by dynamics sketched in Fig. 1A that have until now been largely studied in isolation or under idealized settings.

Our observations of iceberg-scale boundary layers are thicker and more energetic than those simulated in the lab or modelled numerically. Here, rising currents and their turbulence extend 20-50 cm from the ice, contrasting the 1-10 cm lateral scales in simulated flows. And while the strongest temperature anomalies (a proxy for melt buoyancy) are confined within a 1-4 cm e-folding distance from the ice, the heat transport extends far from the boundary. Qualitatively, this is evidenced by the sweeps in T (figure 3), driven by eddies that cyclically advect warm waters toward the boundary and extrude meltwater across the plume on ~ 100 sec timescales. These eddies are responsible for the turbulent heat flux j_q (Fig. 4f).

7 Conclusions

Recent observations of thick meltwater intrusions (Jackson et al., 2020) and unexpectedly high frontal ablation rates (Sutherland et al., 2019) have led to suggestions that Holland and Jenkins (1999) and Jenkins (2011)'s models need to be revisited. Some have suggested transfer coefficients need to be modified (Jackson et al., 2020), others have suggested we need a new empirical model (Schulz et al., 2022), constrained by observations, that is "physically plausible," but not physics based. Neither approach is particularly satisfying because they require arbitrary tuning of coefficients to match observations. The details of the physics are important.

Here we demonstrate the ways in which meltwater buoyancy energizes near-boundary turbulence adjacent to a near-vertical section of an iceberg originating from Xeitl Sít' glacier. Importantly, when external sources of mechanical energy are weak, buoyant convection becomes dominant, driving vertical flows that enhance near-boundary turbulence. While these "meltwater plumes" varied in character, their mean structure was well-described by fits to various powerlaw and exponential functions, and provide a means of quantifying scales of the flow.

While the character of real ambient melt plumes is similar to that predicted by theory (Wells & Worster, 2008), lab (Josberger & Martin, 1981) or numerical simulation (Gayen et al., 2016), the natural flows we observe are significantly more energetic. For example, the sole laboratory study to measure temperature within a turbulent boundary layer adjacent vertical melting ice (Josberger

& Martin, 1981) found turbulent temperature fluctuations to be confined within 2-10 mm of the ice, with fluid outside that layer being quiescent and only occasionally being entrained towards the boundary. In contrast, the boundary layer flows observed here are stronger, broader, and produce higher heat fluxes than these idealized studies.

Our observations confirm that meltwater buoyancy can energize turbulence in the ice-adjacent boundary layer as effectively as a moderate external flow, plausibly driving similar meltrates in both cases. But what sets the TKE, j_q and controls the meltrate? While idealized studies provide some insight and intuition, the feedbacks that control melt cannot be determined from the local dynamics alone. For example, we have shown that a flow – forced ostensibly by the same external conditions – can have dramatically different character (compare Fig. 2 panels a-c with d-f). We hypothesise that the interplay between externally-driven turbulence and meltwater convection is critical to the flow dynamics: both shear and buoyant production influence the coherent structures that are of first order importance of turbulent exchange across this boundary layer. Further direct observations that capture the phenomenology of *real* melt-driven boundary-layers and elucidate the range of dynamical possibilities are critical to inform the next generation of experiments and parameterizations.

8 Open Research

All data are available at the National Snow and Ice Data Center `http://nsidc.org/`

Acknowledgments

This work was funded by the NSF (OPP-2023674) and Keck Foundation. We also thank Bridget Ovall and Lucy Waghorn for providing photographs, and Scott and Julie Hursey and Lila and Grant Trask for support of our field operations in Petersburg Alaska.

References

Bendtsen, J., Rysgaard, S., Carlson, D. F., Meire, L., & Sejr, M. K. (2021). Vertical mixing in stratified fjords near tidewater outlet glaciers along Northwest Greenland. *Journal of Geophysical Research: Oceans*, *126*(8), e2020JC016898.

Carroll, D., Sutherland, D., & Hudson, B. (2016). The impact of glacier geometry on meltwater plume structure and submarine melt in Greenland fjords. *Geophysical Research Letters*, *43*.

Cowton, T., Slater, D., Sole, A., Goldberg, D., & Nienow, P. (2015, feb). Modeling the impact of glacial runoff on fjord circulation and submarine melt rate using a new subgrid-scale parameterization for glacial plumes. *Journal of Geophysical Research: Oceans*, *120*(2), 796–812. Retrieved from `http://doi.wiley.com/10.1002/2014JC010324` doi: 10.1002/2014JC010324

Cusack, J. M., Jackson, R. H., Nash, J. D., Skyllingstad, E., Pettit, E. C., Sutherland, D. A., … Amundson, J. M. (2023). Internal gravity waves generated by subglacial discharge: Implications for tidewater glacier melt. *Geophysical Research Letters*, *50*(12), e2022GL102426.

Eckert, E. R. G., & Jackson, T. W. (1950). Analysis of turbulent free-convection boundary layer on flat plate. *National Advisory Committee on Aeronautics*, *Technical Note 2207*.

Fer, I., McPhee, M. G., & Sirevaag, A. (2004). Conditional statistics of the Reynolds stress in the under-ice boundary layer. *Geophysical Research Letters*, *31*(15).

Gade, H. G. (1979). Melting of ice in sea water: A primitive model with application to the Antarctic ice shelf and icebergs. *Journal of Physical Oceanography*, *9*(1), 189–198.

Gargett, A. E. (1989). Ocean turbulence. *Annual Review of Fluid Mechanics*, *21*(1), 419–451.

Gayen, B., Griffiths, R. W., & Kerr, R. C. (2016, May). Simulation of convection at a vertical ice face dissolving into saline water. *Journal of Fluid Mechanics*, *798*, 284–298.

Holland, D. M., & Jenkins, A. (1999). Modeling thermodynamic ice-ocean interactions at the base of an ice shelf. *Journal of Physical Oceanography*, *29*(8), 1787–1800.

Jackson, R., Nash, J., Kienholz, C., Sutherland, D., Amundson, J., Motyka, R., … Pettit, E. (2020). Meltwater intrusions reveal mechanisms for rapid submarine melt at a tidewater glacier. *Geophysical Research Letters*, *47*(2), e2019GL085335.

Jenkins, A. (2011). Convection-driven melting near the grounding lines of ice shelves and tidewater glaciers. *J. Phys. Oceanogr.*, *41*(12), 2279–2294.

Jenkins, A., Dutrieux, P., Jacobs, S. S., McPhail, S. D., Perrett, J. R., Webb, A. T., & White, D. (2010, jun). Observations beneath Pine Island Glacier in West Antarctica and implications for its retreat. *Nat. Geosci.*, *3*(7), 468–472. Retrieved from `http://www.nature.com/doifinder/10.1038/ngeo890` doi: 10.1038/ngeo890

Josberger, E. G., & Martin, S. (1981). A laboratory and theoretical study of the boundary layer adjacent to a vertical melting ice wall in salt water. *Journal of Fluid Mechanics*, *111*, 439–473.

Kerr, R. C., & McConnochie, C. D. (2015, January). Dissolution of a vertical solid surface by turbulent compositional convection. *Journal of Fluid Mechanics*, *765*, 211–228.

Kimura, S., Holland, P. R., Jenkins, A., & Piggott, M. (2014). The effect of meltwater plumes on the melting of a vertical glacier face. *Journal of Physical Oceanography*, *44*, 3099–3117.

Kline, S. J., Reynolds, W. C., Schraub, F., & Runstadler, P. (1967). The structure of turbulent boundary layers. *Journal of Fluid Mechanics*, *30*(4), 741–773.

MacAyeal, D. R. (1985). Evolution of tidally triggered meltwater plumes below ice shelves. *Oceanology of the Antarctic Continental Shelf*, 133–143.

Macias, J., Bante-Guerra, J., Cervantes-Alvarez, F., Rodrìguez-Gattorno, G., Arés-Muzio, O., Romero-Paredes, H., ... others (2019). Thermal characterization of carbon fiber-reinforced carbon composites. *Applied Composite Materials*, *26*, 321–337.

Magorrian, S. J., & Wells, A. J. (2016). Turbulent plumes from a glacier terminus melting in a stratified ocean. *Journal of Geophysical Research: Oceans*, *121*(7), 4670–4696.

McConnochie, C. D., & Kerr, R. C. (2017, July). Testing a common ice-ocean parameterization with laboratory experiments. *Journal of Geophysical Research Oceans*, *122*(7), 5905–5915.

McPhee, M. G., Maykut, G. A., & Morison, J. H. (1987). Dynamics and thermodynamics of the ice/upper ocean system in the marginal ice zone of the Greenland Sea. *Journal of Geophysical Research*, *92*(C7), 7017–7031.

Parker, D., Burridge, H., Partridge, J., & Linden, P. (2021). Vertically distributed wall sources of buoyancy. Part 1. Unconfined. *Journal of Fluid Mechanics*, *907*, A15.

Perlin, A., Moum, J., Klymak, J., Levine, M., Boyd, T., & Kosro, P. (2005). A modified law-of-the-wall to describe velocity profiles in the bottom boundary layer. *J. Geophys. Res.*, *110*(C10S10). (doi:10.1029/2004JC002310)

Schulz, K., Nguyen, A., & Pillar, H. (2022). An improved and observationally-constrained melt rate parameterization for vertical ice fronts of marine terminating glaciers. *Geophysical Research Letters*, *49*(18), e2022GL100654.

Slater, D., Goldberg, D. N., Nienow, P. W., & Cowton, T. R. (2016). Scalings for submarine melting at tidewater glaciers from buoyant plume theory. *Journal of Physical Oceanography*, *46*, 1839–1855.

Smith, R. R. (1972). *Characteristics of turbulence in free convection flow past a vertical plate.* (Unpublished doctoral dissertation). Queen Mary University of London.

Smyth, W. D. (1999). Dissipation-range geometry and scalar spectra in sheared stratified turbulence. *J. Fluid Mech.*, *401*, 209–242.

Stanton, T. P., Shaw, W., Truffer, M., Corr, H., Peters, L., Riverman, K., . . . Anandakrishnan, S. (2013). Channelized ice melting in the ocean boundary layer beneath Pine Island Glacier, Antarctica. *Science*, *341*(6151), 1236–1239.

Sutherland, D., Jackson, R. H., Kienholz, C., Amundson, J. M., Dryer, W., Duncan, D., . . . Nash, J. (2019). Direct observations of submarine melt and subsurface geometry at a tidewater glacier. *Science*, *365*(6451), 369–374.

Thomson, J., Schwendeman, M. S., Zippel, S. F., Moghimi, S., Gemmrich, J., & Rogers, W. E. (2016). Wave-breaking turbulence in the ocean surface layer. *Journal of Physical Oceanography*, *46*(6), 1857–1870.

Tsuji, T., & Nagano, Y. (1988). Characteristics of a turbulent natural convection boundary layer along a vertical flat plate. *International journal of heat and mass transfer*, *31*(8), 1723–1734.

Watkins, R. H., Bassis, J. N., & Thouless, M. (2021). Roughness of ice shelves is correlated with basal melt rates. *Geophysical Research Letters*, *48*(21), e2021GL094743.

Weiss, K., Nash, J., Wengrove, M., & Others. (2024). Direct measure of melt at an iceberg. *Geophys. Res. Lett.*, *in prep*(0), 00-00.

Wells, A. J., & Worster, M. G. (2008). A geophysical-scale model of vertical natural convection boundary layers. *Journal of Fluid Mechanics*, *609*, 111–137.

Wengrove, M. E., Pettit, E. C., Nash, J. D., Jackson, R. H., & Skyllingstad, E. D. (2023). Melting of glacier ice enhanced by bursting air bubbles. *Nature Geoscience*, *16*(10), 871–876.

Wiles, P., Rippeth, T., Simpson, J., & Hendricks, P. (2006). A novel technique for measuring the rate of turbulent dissipation in the marine environment. *Geophys. Res. Lett.*, *33*(21), L21608.

Xu, Y., Rignot, E., Fenty, I., Menemenlis, D., & Flexas, M. M. (2013). Subaqueous melting of Store Glacier, west Greenland from three-dimensional, high-resolution numerical modeling and ocean observations. *Geophysical Research Letters*, *40*(17), 4648–4653.

Zhao, K., Skyllingstad, E., & Nash, J. (2024). Improved parameterizations of vertical ice-ocean boundary layers and melt rates. *Gephys. Res. Lett*, *in press*.

Zhao, K., Stewart, A., McWilliams, J., Fenty, I., & Rignot, E. (2023). Standing eddies in glacial fjords and their role in fjord circulation and melt. *Journal of Physical Oceanography*, *53*(3), 821–840.

Supplement to "Turbulent Dynamics of Buoyant Melt Plumes Adjacent Near-Vertical Glacier Ice"

S1 Assessing the Structure of the Thermal Boundary Layer

Eight fast-response thermistors distributed along the thermistor rake (or T-rake) and three RBR-solos create a timeseries of T at 11 locations that are used to image the turbulent near-boundary flow and to characterize scales of time-averaged temperature. On the T-rake, the thermistors (1.65 mm diameter, epoxy-encased Amphenol 10 kOhm 527-MC65F103B) are directly exposed to seawater and protrude out the side of a 4-mm carbon fiber tube with a goal of sampling the mean and fluctuating turbulent T with minimal contamination. Thermistors were mounted at distances of 2, 4, 7, 12, 23, 39, 58 and 84 mm from the tube's tip (Fig. S1), and the sensors were oriented downward in anticipation of the mean buoyant flow being positive vertical. The roughly logarithmic spacing was chosen because of our expectation that temperature gradients increase with proximity to the boundary.

The thermistors were sampled at 100 Hz using 16-bit electronics adapted from Moum and Nash (2009) yielding 0.5 mK precision and < 2 mK accuracy over the calibrated $0-10$ C range. A $1/e$ time constant ($\tau = 0.2$ sec) was measured during dip tests in the lab; in the field their response was slower ($\tau \sim 1$ sec), likely due to thermal mass effects associated with their mounting configuration.

We attempted to deploy the Meltstake so that the thermistor rake was approximately perpendicular to the ice face, and as close to the ice as possible. At times, we believe the T-rake was in contact with the ice immediately following a drilling / Meltstake advance sequence. One challenge with these measurements is determining the distance between ice and T-rake tip (y_o), as this was not measured independently. In this section, we show how the various functional forms for the mean temperature structure are related, and in doing so, also outline our procedure for estimating the T-rake location (y_o, its distance from the ice).

There are no previous measurements of temperature in the boundary layer adjacent a rough, melting, near-vertical ice interface. Here we start with the similarity solution of Eckert and Jackson (1950) which was effective in describing the velocity structure of the plumes (Fig. 3). While it was initially derived for aerospace applications (and $Pr = 1$), it also provides an empirical form for the temperature profile (their equation 4 and figure 2):

$$\theta = \theta_w \left[1 - \left(\frac{y}{\delta} \right)^{1/7} \right] \tag{S1}$$

where θ is the temperature anomaly associated with the plume, θ_w is the temperature difference between wall and outer flow, and δ is the boundary layer thickness. However, this form (and the data on which it was based) used air for the fluid and assumed the Prandtl number equals one. As a result, the boundary layer thickness (that governs the decay scale) for θ is the same as that for w (δ and $L_w = 0.304\delta$). While it has been applied to the ice-ocean boundary to interpret numerical simulations (Parker et al., 2021; Zhao et al., 2024), it is not expected to adequately represent the flow very near the ice, which differs from the assumed setting in at least two ways: (1) from a diffusivity standpoint (the molecular diffusivities for heat D_T and salt D_S are 10-1000 times smaller than the molecular viscosity ν), and (2) because of the possibility that ice-roughness may strongly modify the near-boundary flow. As a result, we hypothesize that their form will be most relevant far from the boundary, and consider a slightly modified version of equation (S1) to describe the outer layer. We define:

$$\widehat{T} = T_a - \Delta T \left[1 - \left(\frac{y}{\delta} \right)^{1/7} \right], \tag{S2}$$

Figure S1. Configuration of thermistors on the T-rake; calipers provide scale. All 16 electrical leads are fed through the carbon tube, within which they transition to larger diameter copper wire; the entire assembly is then filled with a low-viscosity polyurethane adhesive to make the assembly waterproof. Newer versions of the T-rake have the Amphenol 527-MC65F103B sensing elements offset from the carbon tube an additional 3mm to provide better exposure to the turbulent flow. The thermistors in that configuration are supported by adhesive-filled heat-shrink tubing, which provides mechanical support, insulates the electrical leads, and thermally isolates the sensors from the carbon support tube.

in which δ is the same as Eckert and Jackson (1950)'s δ and computed by fitting $\widehat{w}$ to the vertical velocity profile (equation (1)). We introduce ΔT to represent the temperature drop through the outer (turbulence dominated) boundary layer, but not including the inner, diffusive layer over which the temperature drops to freezing, and where differences between D_T, D_S and ν will be most important. In Eckert and Jackson (1950)'s original form, there is no ΔT: ΔT was set to equal T_a in order for $\widehat{T}$ to reach 0° C at the boundary. However, if we use their form and set $\Delta T = T_a$, the predicted temperature is far too diffuse (and colder) than that observed. We demonstrate this in the upper panels of figure S2, where the thin dotted lines are $\widehat{T} = T_a - T_a(1-(y/\delta)^{1/7})$. Hence, the lengthscale L_w (and δ) derived from our fits of $\widehat{w}$ to w does not characterize total temperature drop from ambient (T_a) to ice assuming this functional form.

Here we recognize that Eckert and Jackson (1950)'s Prandtl number assumption ($Pr = 1$) is not expected to be valid here, and especially near the ice interface where molecular processes (and differences between D_T and ν) control transports across the viscous sublayer. In this region, we should not expect δ – the scale derived from $w(y)$ and associated with momentum transports by the turbulent stress – to be appropriate. For this reason we introduce a second length scale, L_T, relevant to $T(y)$ as $y \to 0$, used to characterized the inner sublayer that results from an interplay between molecular and turbulent processes that diffuses the buoyant meltwater and its thermal signature. We envision this sublayer as a way of connecting the outer boundary layer region – controlled by plume turbulence and described by eq. (S2) and δ – to the boundary, so that only a small fraction of the temperature drop occurs in the outer region (as we observe). For this reason we introduced ΔT in eq. S2 and perform a least-squares minimization to the outer 5 temperature measurements. We find (fig. S2) that T in the outer boundary layer is approximately represented by this model (heavy dotted lines). From these fits, $\Delta T \sim 1°$ in each case, which corresponds to a 0.2-0.3 °C temperature drop in the outer boundary layer where the model best represents the data.

In this hybrid model, most of the temperature drop must occur within the inner boundary layer, for which we propose T approximately follows an exponential function of the form

$$\widehat{T}(y) = T_a - (T_a - T_i)e^{-y/L_T}. \tag{S3}$$

Here, T_a is the ambient (farfield) temperature and T_i is the water temperature on the ocean side of the ice interface, and L_T is a thermal-diffusive lengthscale. We note that laboratory experiments (Josberger & Martin, 1981; McConnochie & Kerr, 2017) suggest that $T_i = -0.5°$C; however, to simplify equation S3, we assume $T_i = 0^\circ$ C (equal to the ice temperature); this assumption has little effect on our results. To determine T_a, L_T and y_o (the offset of the T-rake from the ice), we minimize $\sum_{n=1}^{8}(T(y_n) - \widehat{T}(y_n))^2$ for each of the n thermistors, with $y_n = y_o + y'_n$, where y'_n is the location of each sensor relative to the T-rake tip[1]. In the present configuration of the Meltstate, the T-rake is at a fixed location relative to the iceberg, and as a result, as the ice

[1] We determine fits to the data by minimizing the squared residual between model and data using the Levenberg-Marquardt nonlinear least squares algorithm as implemented in Matlab's nlinfit.m (Seber & Wild, 2003).

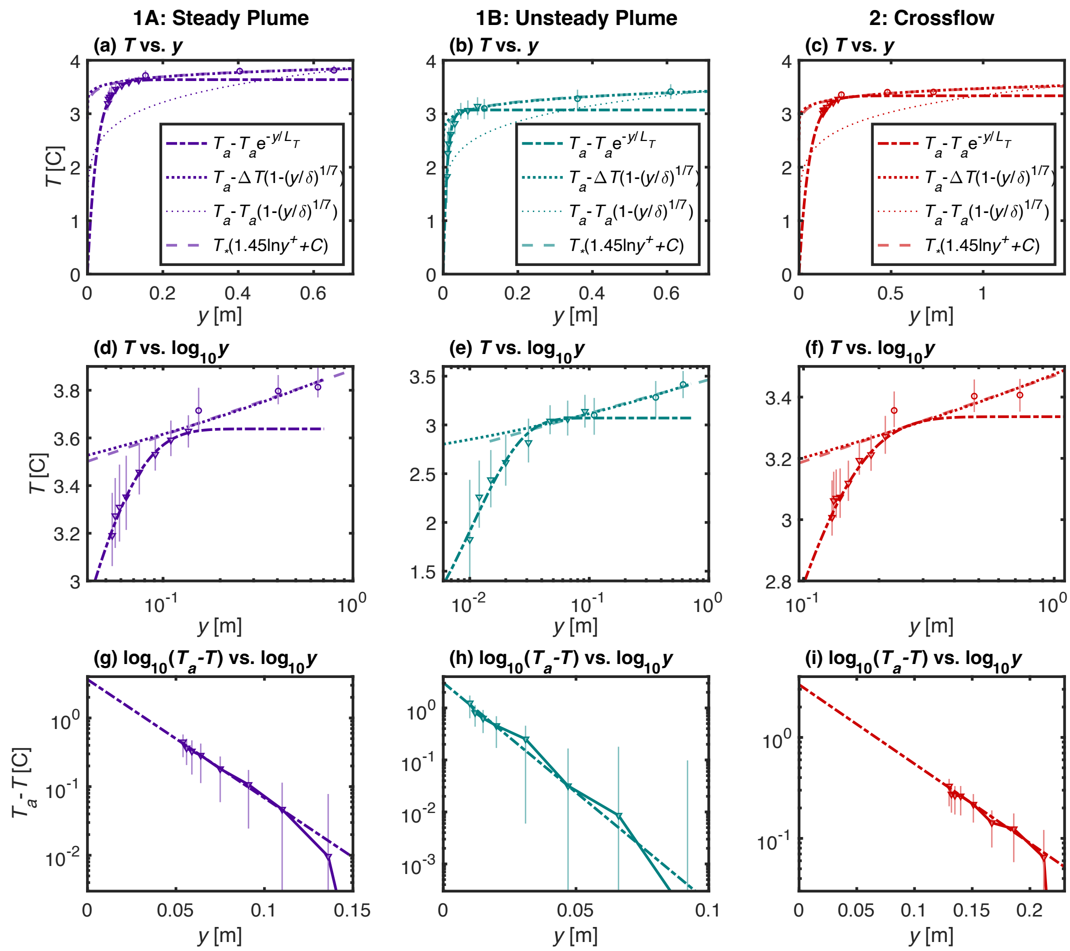

Figure S2. Mean character of the observed thermal boundary layer. Data are the same as in fig. 3c, but separated into the three individual periods: Case 1A: 29-May-2023 20:40-21:00 (a,d,g); Case 1B: 29-May-2023 23:06:45-23:26:45 (b,e,h); and Case 2: 30-May-2023 01:48-02:05 (c,f,i). Each row presents the data with different axes (linear-linear, linear-log, and log-log) to highlight the character of each layer and corresponding fit. The dash-dot lines represent fits in the inner sublayer (equation S3), the heavy dotted lines represent the fit to the modified Eckert and Jackson (1950) form (equation S2), and the light dotted lines are Eckert and Jackson (1950)'s original form (equation S1).

	Outer boundary layer Eckert & Jackson (1950)			Inner boundary layer Exponential fit			Transition Distance
Case	T_a [°C]	ΔT [°C]	δ [cm]	T_a [°C]	L_T [cm]	y_o [cm]	L_{out} [cm]
1A	3.85	0.95	70	3.64	2.5	5.4	1.5
1B	3.42	1.25	71	3.07	1.0	1.0	2.1
1B (10 min)				3.12	0.8	0.5	
1B (5 min)				3.0	0.6	0.2	
2	3.53	1.02	144	3.34	5.5	13	3.2

Table S1. Coefficients for empirical forms presented in Fig. S2. Case 1B (10 min) and (5 min) represents the coefficients computed from the first 10 and 5 minutes respectively. L_{out} is the distance at which $y^+ = 30$, and represents the outer scale of the transition layer and a measure of the maximum extent of viscous boundary effects.

melts, y_o increases in time. For this reason, we choose relatively short (20 min) periods for these calculations, and assume y_o is constant over each period.

For completeness, we also include a formulation for the boundary layer's thermal structure presented in Tsuji and Nagano (1988) that relaxes the assumption of $Pr = 1$. Here we follow their conventions and define the dimensionless distance from the wall as $y^+ = u_* y/\nu$, where $u_* = \sqrt{\tau_w/\rho}$ is the friction velocity that is derived from equation (4) using our fit to the vertical velocity profile. Hence, y^+ is based on the momentum scaling. They also define the dimensionless temperature $T^+ = (T - T_i)/T_*$ where T_* is the "friction temperature" and T_i is the temperature at the wall. Their formation also breaks the boundary layer into two sub-regions: (1) a viscous sublayer very close to the wall (valid for distances $0 < y^+ < 5$), where T varies linearly with y such that $T^+ = Pry^+$, and (2) an outer turbulent layer (valid for distances of $30 < y^+ < 200$), for which

$$T^+ = 1.45 \ln y^+ + C. \tag{S4}$$

We apply this equation to our observations by fitting equation S4 to data from the outer five sensors[1]. In their formulation there is a transition layer between these two regions ($5 < y^+ < 30$), which depends on details of flow development (and the Grashof number), which we do not investigate here. However, because of the importance of y^+ in delineating the inner and outer boundary layers, we define $L_{out} = 30\nu/u_*$ as the distance where the outer (turbulence-dominated) boundary layer dynamics are at play. We also note that Tsuji and Nagano (1988) found experimental agreement primarily within the inner sublayer; significant deviation was observed when comparing equation S4 to experimental observations of the outer boundary layer. We note, however, that few data were acquired in an aquatic environment.

To demonstrate the differences in boundary layer shapes, we present each of these fits in figure S2. We present the same data (and fits) on three separate plots using different axes (linear-linear, linear-log, and log-log) to highlight the shape of each function and its relation to the data in the two different boundary layer regions. The upper two rows of plots show how the outer sensors are well represented by our modified version of Eckert and Jackson (1950)'s model and equation (S2). Our data are also consistent with Tsuji and Nagano (1988)'s formulation, which is largely indistinguishable from Eckert and Jackson (1950)'s in the outer layer. In contrast, the inner boundary layer closely follows the exponential form presented in equation (S3), which is highlighted in the bottom rows. We find that the inner plume thermal-diffusive lengthscales ($L_T = 1 - 4$ cm) are a factor of ten smaller than L_w ($= 25 - 50$ cm), and that both scales are largest during periods of strong crossflow (case 2).

Note that in case 1B (in particular), the T-rake was very close to the ice, so the change in y_o over the 20 min period during which the mean is computed turns out to be an appreciable fraction of y_o. Because of this, we also perform the exponential fit calculations using shorter subsets of the data (the first 5- and 10-min) that correspond to the subsets of data presented in Figure 3. During this time, we find that y_o increases monotonically, such that $y_o = 2$ mm when computed over the first 5-min period, $y_o = 5$ mm when computed over the first 10 min, and $y_o =$ 10 mm when computed over the entire 20 min. Thus, the innermost T-rake thermistor was on average 4 mm from the ice during the first five minutes, increasing to 7 mm over the next five minutes. That sensor recorded 0° C during three meltwater ejection events, each separated $\sim$100 seconds in time. During these first 5-min, the temperature decay scale was $L_T = 6$ mm, slightly smaller than the 20-min average ($L_T = 10$ mm). A summary of all fits is shown in Table S1.

References

Eckert, E. R. G., & Jackson, T. W. (1950). Analysis of turbulent free-convection boundary layer on flat plate. *National Advisory Committee on Aeronautics*, *Technical Note 2207*.

Josberger, E. G., & Martin, S. (1981). A laboratory and theoretical study of the boundary layer adjacent to a vertical melting ice wall in salt water. *Journal of Fluid Mechanics*, *111*, 439–473.

McConnochie, C. D., & Kerr, R. C. (2017). Enhanced ablation of a vertical ice wall due to an external freshwater plume. *Journal of Fluid Mechanics*, *810*, 429–447.

Moum, J. N., & Nash, J. D. (2009). Mixing measurements on an Equatorial ocean mooring.

Journal of Atmospheric and Oceanic Technology, *26*, 317–336.

Parker, D., Burridge, H., Partridge, J., & Linden, P. (2021). Vertically distributed wall sources of buoyancy. Part 1. Unconfined. *Journal of Fluid Mechanics*, *907*, A15.

Seber, G. A., & Wild, C. J. (2003). Nonlinear regression. *New Jersey: John Wiley & Sons*, *62*(63), 1238.

Tsuji, T., & Nagano, Y. (1988). Characteristics of a turbulent natural convection boundary layer along a vertical flat plate. *International journal of heat and mass transfer*, *31*(8), 1723–1734.

Zhao, K., Skyllingstad, E., & Nash, J. (2024). Improved parameterizations of vertical ice-ocean boundary layers and melt rates. *Gephys. Res. Lett*, *in press*.